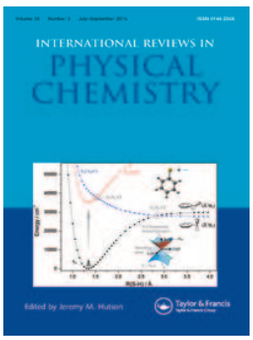

International Reviews in Physical Chemistry

ISSN: 0144-235X (Print) 1366-591X (Online) Journal homepage: http://www.tandfonline.com/loi/trpc20

Structure and dynamic role of conical intersections in the πσ*-mediated photodissociation reactions

Hyun Sik You, Songhee Han, Jun-Ho Yoon, Jeong Sik Lim, Jeongmook Lee, So-Yeon Kim, Doo-Sik Ahn, Jean Sun Lim & Sang Kyu Kim

To cite this article: Hyun Sik You, Songhee Han, Jun-Ho Yoon, Jeong Sik Lim, Jeongmook Lee, So-Yeon Kim, Doo-Sik Ahn, Jean Sun Lim & Sang Kyu Kim (2015) Structure and dynamic role of conical intersections in the πσ*-mediated photodissociation reactions, International Reviews in Physical Chemistry, 34:3, 429-459

To link to this article: http://dx.doi.org/10.1080/0144235X.2015.1072364

Published online: 12 Oct 2015.

International Reviews in Physical Chemistry, 2015
Vol. 34, No. 3, 429–459, http://dx.doi.org/10.1080/0144235X.2015.1072364

Structure and dynamic role of conical intersections in the πσ*-mediated photodissociation reactions

Hyun Sik You[a], Songhee Han[b], Jun-Ho Yoon[a], Jeong Sik Lim[c], Jeongmook Lee[d], So-Yeon Kim[a], Doo-Sik Ahn[a], Jean Sun Lim[a] and Sang Kyu Kim[a]*

[a]*Department of Chemistry, KAIST, Daejeon 305-701, Republic of Korea;* [b]*Max-Born-Institute for Nonlinear Optics and Short Pulse Spectroscopy in Berlin Research Association, Max-Born-Str. 2A, 12489 Berlin, Germany;* [c]*Korea Research Institute of Standards and Science, Daejeon, Republic of Korea;* [d]*Korea Atomic Energy Research Institute, Daejeon, Republic of Korea*

(*Received 14 October 2014; final version received 9 July 2015*)

Conical intersection as a dynamic funnel in nonadiabatic transition dictates many important chemical reaction outputs such as reaction rates, yields, and energy disposals especially for chemical reactions taking place on electronically excited states. Therefore, the energetics and topology of conical intersections have been subjected to intensive theoretical and experimental studies for decades as these things are the keys to understanding and controlling nonadiabatic transitions which are ubiquitous in nature. In this article, we focus on πσ*-mediated photodissociation reactions of thiophenols and thioanisoles. Interestingly, for these chemical systems, the nonadiabatic transition probability can be precisely measured as a function of the excitation energy, giving a great opportunity for spectroscopic characterization of the multi-dimensional conical intersection seam that governs the nonadiabatic transition dynamics of polyatomic molecules. The passage of the reactive flux in the proximity of the conical intersection gives rise to dynamic resonances corresponding to dramatic state-specific increases of the nonadiabatic transition probability. Accordingly, it is found that the electronic and nuclear configurations of the reactive flux and their evolution, coupled to the conical intersection seam, are critical in nonadiabatic transition dynamics. Nonadiabaticity is found to be extremely sensitive to the conformational molecular structure, and this has been demonstrated in the photodissociation dynamics of the chemical derivatives of thiophenol. Intramolecular vibrational redistribution, which is nontrivial in surmounting the reaction barrier, is found to wash out state-specific dynamic resonances, implying the importance of the dynamic interplay between vibrational energy flow and nonadiabatic transition. The experimental results on conical intersection dynamics presented in this review provide many interesting and important issues to be pursued in the near future by both theoreticians and experimentalists.

Keywords: conical intersection; photodissociation; nonadiabatic transition; thiophenol; thioanisole

Contents

*Corresponding author. Email: sangkyukim@kaist.ac.kr

1. Introduction: dynamics beyond the Born–Oppenheimer approximation

Chemical reactions are often envisioned as nuclear rearrangements destined to move on pre-determined electronic potential energy surfaces. This adiabatic picture relies on the Born–Oppenheimer approximation, which assumes that nuclear motion is separable in time from the much faster electronic motion. The Born–Oppenheimer approximation has been enormously successful in describing chemical reactions on the ground electronic state [1]. For chemical reactions taking place on electronically excited states, however, dynamic coupling of electronic and nuclear motions is nontrivial, and thus nonadiabatic transitions become significant in many circumstances [2,3]. Actually, nonadiabatic transitions are ubiquitous in nature and even essential in some important chemical and biological processes [4–17]. These include photoisomerization as an initial impulse in the vision process [18,19], ultrafast nonradiative relaxation of DNA bases to protect their genetic information against external deep-UV irradiation [4,20–23], and photocatalytic reactions [24,25] that are essential in light-harvesting systems. Nonadiabatic dynamics have been extensively and intensively investigated both experimentally and theoretically in recent decades, and there are already many excellent review articles dealing with this important subject [2,3,26–28]. In this article we do not intend to review all relevant previous work. Rather, we will focus on recent scientific findings, which have been made mainly at our own laboratory. It should be emphasised here that this article is very likely to be quite incomplete in citing many important works in this field.

The nonadiabatic transition has been nicely visualised in the marvellous femtosecond time-resolved experiment of Zewail and colleagues, showing wavepacket motion bouncing back and forth with finite penetrating probability against the adiabatic wall that is generated by the avoided crossing in the photodissociation reaction of diatomic molecules such as NaI [29–33]. For polyatomic molecules, however, the situation is somewhat different. The non-crossing rule does not strictly apply to polyatomic molecular systems as the number of internal degrees of freedom increases. Actually, a conical intersection point is generated by the intersection of two potential surfaces on

the two-dimensional branching plane [34–41]. Naturally, the conical intersection lies on the (3N−8) dimensional seam where (3N−6) is the number of internal degrees of freedom of the N-atomic molecular system [28,42,43]. As the energy gap between two adiabats becomes infinitesimally small in the proximity of conical intersections, nonadiabatic transitions become most efficient when the reactive flux or wavepacket reaches the conical intersection region during the chemical reaction process. For diatomic molecules, the interatomic distance is the only parameter in the chemical reaction, and the nonadiabatic transition probability is maximised when the wavepacket reaches the avoided-crossing region along the interatomic distance. For polyatomic molecular systems, however, nonadiabatic dynamics are much more complicated as the nuclear and electronic configurations are multi-dimensional in nature. High-level theoretical calculations of the conical intersection are thus often limited to small molecular systems. For large chemical systems, the dimensionality should be reduced for potential energy surface calculations and wavepacket simulations. Experimental characterization of the multi-dimensional conical intersection is also a formidable task, though it would be extremely valuable if one could figure out the structure and dynamic role of conical intersection as most dynamic variables of nonadiabatic transitions are determined by the nature of the conical intersection.

It might be fair to state that the conical intersection, in terms of its topology and dynamic role, can be understood to some extent for certain chemical and biological processes thanks to the many beautiful theoretical and experimental studies from prominent worldwide research groups. Spectroscopic perturbations reflecting distorted potential energy surfaces caused by the conical intersection have been observed for some simple chemical systems such as ozone [44–46]. The speed and angular distributions of nascent products from a number of different photodissociation reactions have been measured to reveal the dynamic role of conical intersections along the reaction pathway [47–52]. Energy and/or mode selective photodissociation studies have been intensively conducted and have provided valuable information about the dynamic role of the conical intersection for a variety of chemical systems [53–56]. Real-time wavepacket dynamics in the femtosecond time resolution have been studied to visualise the surface hopping mechanism in some important chemical and biological processes [18,57–60]. The time-resolved photoelectron spectroscopic method has been very successfully employed to provide deep insight into nuclear and electronic configurations involved in nonradiative transitions near the conical intersection [9,10,61–65]. Despite the many important and successful studies regarding the conical intersection to date, however, it remains a difficult challenge to experimentally unravel the structural and dynamic role of the multi-dimensional conical intersection.

Recently, our group reported a promising result in this endeavour. Namely, in the S–CH_3 bond dissociation of thioanisole ($C_6H_5SCH_3$) [66], it was found that the nonadiabatic transition probability shows a resonance-like feature at certain vibronic excitations of the reactant. According to the theoretical concept of the conical intersection, the nonadiabatic transition probability is expected to be increased when the reactive flux or a wavepacket reaches a conical intersection region. Therefore, the experimental fact that the nonadiabatic transition becomes more efficient at a specific vibronic transition, for instance, indicates that the initial reactive flux prepared by the corresponding optical excitation directly accesses the nuclear configuration in the proximity of the conical intersection. This observation could be a first step toward the spectroscopic characterization of the conical intersection in terms of its multi-dimensional topology and energetics. First, we will briefly review the πσ*-mediated photodissociation reactions of

heteroaromatic molecular systems [67]. All of the relevant works [66,68–75] from our group on conical intersections are in some sense extensions of the pioneering experimental works of Ashfold and colleagues and the theoretical works of Sobolewski, Domcke, and many others on a number of interesting πσ*-mediated photochemical systems. Experimental findings from our laboratory, however, are unique as we have been able to probe the conical intersection region via the measurement of dynamic variables, providing spectroscopic characterization of the multi-dimensional conical intersection seam for the first time. Our results at the same time give rise to many challenging and exciting issues that should be interesting and worthwhile to pursue for both experimentalists and theoreticians. We will provide here a comprehensive story about the photodissociation reactions of thiophenol [68,69,72], thioanisole [66,73], and their chemical derivatives [70,75], as far as we understand those reactions at the present time.

2. Nonadiabatic transitions in πσ*-mediated photodissociation reactions

The photochemistry of aromatic molecules has been an attractive subject to chemical physicists for the past several decades. This is partly because simple aromatic molecules are ideal model systems for the investigation of the photobiological and photochemical processes that are ubiquitous in nature [24,76–78]. Detailed understanding of the energy flow mechanism in photo-excited aromatic molecular systems, for instance, is not only fundamentally interesting but also quite useful in practical applications of organic devices [24,79] in solar energy conversion. One of recent and arguably most-spotlighted subjects in this endeavour is the photochemistry of hetero-aromatic molecules [80]. In hetero-aromatic molecules, a hetero-atom (X = N, S, O) is either attached to the phenyl moiety with a chemical form of XH (or XCH_3) or engaged in the π-conjugation of the aromatic ring. The most intriguing characteristic of these photochemical systems is that the bond dissociation along X–H or X–CH_3 occurs through the repulsive πσ* state which is strongly coupled to the close-lying ππ* bound state which is intrinsically aromatic. The conical intersection of the bound ππ* and the repulsive πσ* states then play important roles in the nonadiabatic transitions involved in internal conversions and/or bond cleavage reactions. Particularly, the role of the πσ* state in the efficient nonadiabatic transitions of biological building blocks such as DNA bases has been intensively investigated since the pioneering work [4] of Sobolewski, Domcke, Dendonder-Lardeux, and Jouvet. Meanwhile, photodissociation reactions of hetero-aromatic systems including NH (or N–CH_3), OH (or O–CH_3), or SH (or S–CH_3) such as phenols [81–95], anisoles [96,97], anilines [48,98–102], pyrroles [103–111], thiophenols [68–70,72,75,112–115], and thioanisoles [47,66,73] have also been extensively and intensively studied. The Ashfold group has reported many significant works on these systems using high-resolution Rydberg-tagged photofragment translational spectroscopy [116]. Recent time-resolved works [117] by the Stavros group are also quite noteworthy as they reveal the other side of the coin of the conical intersection. As a matter of fact, the photochemistry of various hetero-aromatic molecules has already been comprehensively reviewed by the Ashfold group [67], and one should refer to those reviews for further detail.

3. The πσ*-mediated S–H (CH_3) bond dissociation dynamics and conical intersections

The photochemistry of thiophenol and thioanisole has the common feature of the πσ*-mediated photodissociation reaction of hetero-aromatic systems. Namely, two

conical intersections are encountered along the reaction pathway leading to the S–H or S–CH_3 bond fragmentation of electronically-excited states of thiophenol or thioanisole, respectively. At the planar geometry, the first conical intersection is generated by crossing of the S_1 bound ($\pi\pi^*$) and upper-lying repulsive S_2 ($\pi\sigma^*$) states [69,70]. At the later stage of the reaction pathway, the second conical intersection is formed as a result of curve crossing of the S_2 and S_0 states, as S_2 correlates with the ground $C_6H_5S\cdot$ radical whereas S_0 correlates with the excited $C_6H_5S\cdot$ radical diabatically at the asymptotic level, as can be seen in Figure 1. Accordingly, the reactive flux riding on the repulsive S_2 state gives rise to the first electronically-excited ($\tilde{A}^2B_2$) $C_6H_5S\cdot$ radical adiabatically, whereas the ground ($\tilde{X}^2B_1$) $C_6H_5S\cdot$ radical is produced by nonadiabatic transition at the second conical intersection. One of the outstanding characteristics of thiophenol (or thioanisole) photochemistry is that the energy gap between two distinct product channels at the asymptotic level is quite small even though they are electronically different states [118]. The energy separation between the first electronically-excited ($\tilde{A}^2B_2$) and the ground ($\tilde{X}^2B_1$) states of the $C_6H_5S\cdot$ fragment is only ~3000 cm^{-1} [119]. The difference in the electronic configurations of the $\tilde{A}$ and $\tilde{X}$ states of the $C_6H_5S\cdot$ radical originates from the different alignments of their singly-occupied molecular orbital (SOMO), which is localised on the sulphur atom with respect to the plane of symmetry [68]. The SOMO is aligned perpendicular to the molecular plane in the ground $C_6H_5S\cdot$ radical, whereas it is parallel to the molecular plane in the $\tilde{A}$ state of $C_6H_5S\cdot$. This subtle difference lead to completely different symmetry properties of the two states. Both product channels are energetically accessible even at the zero-point energy (ZPE) level of the first electronically excited state of thiophenol or thioanisole, making feasible an exploration of the many quantum states of the initial reactive flux in terms of their nonadiabatic transition probabilities by measuring product state distributions from the

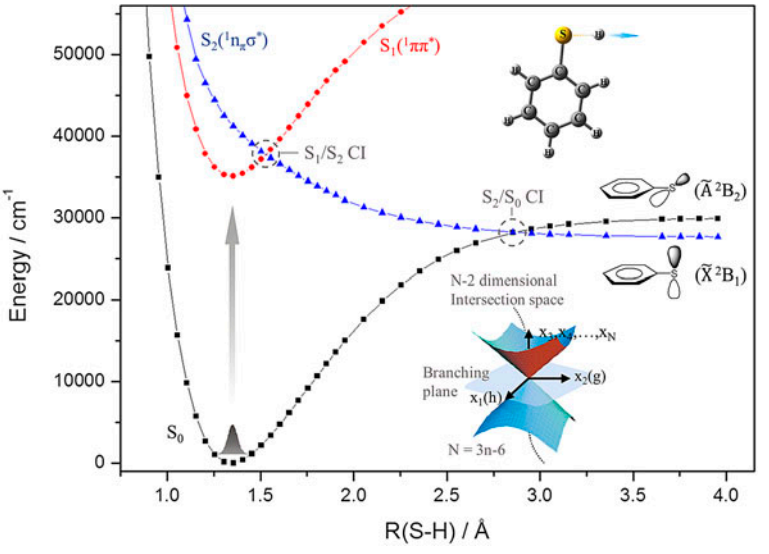

Figure 1. The diabatic potential energy surfaces (S_0, $1^1\pi\pi^*$, and $^1n_\pi\sigma^*$) of thiophenol along the S–H bond elongation coordinate at the planar geometry, obtained by the CASPT2//SA4-CASSCF (12,11)/6–311++G(d,p) level. The two dimensional branching plane of the gradient difference (*g*) and nonadiabatic coupling (*h*) vectors parallel to specific nuclear motions provides a platform for the conical intersection seam generated along the ($N^{int}-2$) dimensional intersection space.

various vibronic states of thiophenol or thioanisole. Nonadiabatic transition probability at the second conical intersection can be precisely estimated from the translational energy distribution of fragments. More specifically, the energy available for the translational energy of the fragments is relatively larger for the nonadiabatic channel leading to the $C_6H_5S\cdot(\tilde{X}^2B_1)$ radical compared to that for the adiabatic channel giving the $C_6H_5S\cdot(\tilde{A}^2B_2)$ radical as a final product. This simple energetic difference between nonadiabatic and adiabatic channels is reflected in the product state distribution of H or of the CH_3 fragment, which is bimodal in shape. The product branching ratio of $C_6H_5S\cdot(\tilde{X}^2B_1)$ with respect to $C_6H_5S\cdot(\tilde{A}^2B_2)$ is proportional to the nonadiabatic transition probability. Therefore, one can estimate the state-specific nonadiabatic transition probability by analysing the bimodal-shaped translational energy distribution of the products.

Dynamics experiments have been carried out using the velocity-map ion imaging technique [120–123] combined with a supersonically-cooled molecular beam. Detailed experimental conditions and methods have been described in previous publications [69,124] from our group. Generally, raw images are reconstructed using the Basex [125] or pBasex [126] algorithm to give the translational energy and angular distributions of the nascent H or CH_3 fragments from thiophenol or thioanisole, respectively, excited at specific S_1 or S_2 vibronic states. For most of thiophenol experiments, the SH group is isotopically substituted to SD so that the experimental result is not interfered by H fragmentation from the benzene moiety of thiophenol. For mode assignments of S_1 vibronic bands of reactants, especially when those are well resolved, we have employed the mass-analysed threshold ionisation (MATI) spectroscopic method [127,128] and/or the slow-electron velocity-map imaging (SEVI) technique [129]. Since the photo-ionisation process is prompt, both MATI and SEVI ionisation spectra reflect the nuclear configuration spanned by a specific S_1 vibronic state used as an intermediate in the $(1 + 1')$ two-colour two-photon ionisation scheme [130,131]. Since *ab initio* calculations are much more reliable for cationic ground states than they are for neutral electronically-excited states, the proper S_1 mode assignment can be accomplished especially when the propensity rule of $\Delta\upsilon = 0$ in the ionisation is followed. Namely, when the molecular structure remains unaltered upon ionisation, only one vibrational band in the cationic ground state is strongly observed in the MATI or SEVI spectrum taken via a specific S_1 intermediate state excitation. Mode assignment of MATI or SEVI band observed using a comparison with theoretical calculations then naturally leads to the proper mode assignment of the S_1 vibronic band. This scheme makes the S_1 vibronic mode assignment reliable, which process is otherwise quite difficult and can often lead to misleading results in many cases. It is also noteworthy that SEVI and/or MATI spectra provide valuable information about the dynamics of vibronic mode-mixing, such as the intramolecular vibrational redistribution (IVR) occurring in the excited states. [132,133]

3.1. *Thiophenol: ultrafast bond rupture dynamics*

The S–H bond dissociation of thiophenol on the S_1 state is prompt. In order to obtain the S_1 vibronic structure of thiophenol, the C_6H_5S fragment is directly ionised by the vacuum ultraviolet laser pulse at 9.6 eV, as shown in Figure 2. The resultant $C_6H_5S\cdot^+$ ion fragment is monitored as a function of the S_1–S_0 excitation energy of thiophenol to obtain the photofragment excitation (PHOFEX) spectrum. As the quantum yield for the S–H bond cleavage is expected to be unity, the PHOFEX spectrum represents the

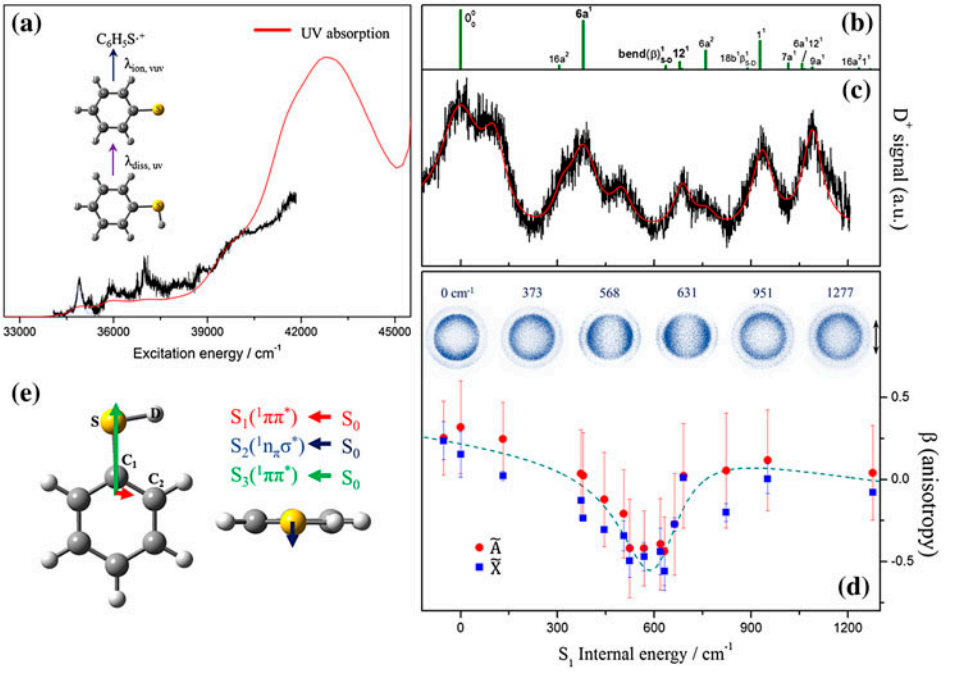

Figure 2. (a) PHOFEX spectrum (black solid line) of thiophenol monitoring the thiophenoxyl radical fragment yield as a function of the photodissociation excitation energy compared with the liquid UV absorption spectrum taken in *n*-hexane (red solid line). The origin band (blue dotted line) was fitted to convolution profile (Voigt profile) of Lorentzian function and Gaussian width that corresponds to the rotational contour (at $T_{rot} = 10$ K) and laser bandwidth. (b) Franck-Condon simulation of the S_1–S_0 transition obtained using TDDFT (B3LYP)/aug-cc-pVTZ. Vibrational mode assignments are also given. (c) PHOFEX spectrum (black solid line) of thiophenol-d_1 monitoring the D fragment yield with a fit (red solid line). (d) The anisotropy parameter (β) values averaged over the FWHM of the translational energy peak associated with the $\tilde{X}$ (blue filled squares) or $\tilde{A}$ (red filled circles) state of the thiophenoxyl radical. The images at specific S_1 internal energies are shown. The black arrow indicates the polarisation direction of the pump laser pulse. (e) Calculated transition dipole moment(TDM) vectors for the first three singlet electronic transitions of thiophenol, calculated at TD-HCTH/aug-cc-pVTZ level. The magnitude of the $S_2(^1n_\pi\sigma^*) \leftarrow S_0$ TDM vector is scaled by a factor of ×2 relative to the $S_1(^1\pi\pi^*) \leftarrow S_0$ and $S_3(^1\pi\pi^*) \leftarrow S_0$ TDM vectors for clarity.

energy-dependent S_1–S_0 absorption cross section. Individual vibronic bands are found to be very broad, indicating that the lifetime of S_1 is ultrashort. The full-width at half-maximum of the S_1 origin band is around 190 cm^{-1}, which corresponds to a lifetime of ~50 fs. This means that the S–H bond dissociation is prompt and energy randomization does not occur prior to the bond cleavage. The S–D bond dissociation of thiophenol-d_1 (C_6H_5SD) is not much different from the S–H bond rupture of thiophenol. The PHOFEX spectrum taken by probing the D fragment also shows very broad spectral features and this is quite consistent with the results reported by the Ashfold group [113], as can be seen in Figure 2. Velocity-map ion images of the D fragment from thiophenol-d_1 taken at various pump energies show bimodal-shaped translational energy distributions. Total translational energy distribution is well separated by deconvolution into two distinct Gaussian-shaped distributions, as can be seen in Figure 3. Obviously, from a simple consideration of energetics, a distribution with larger translational energy

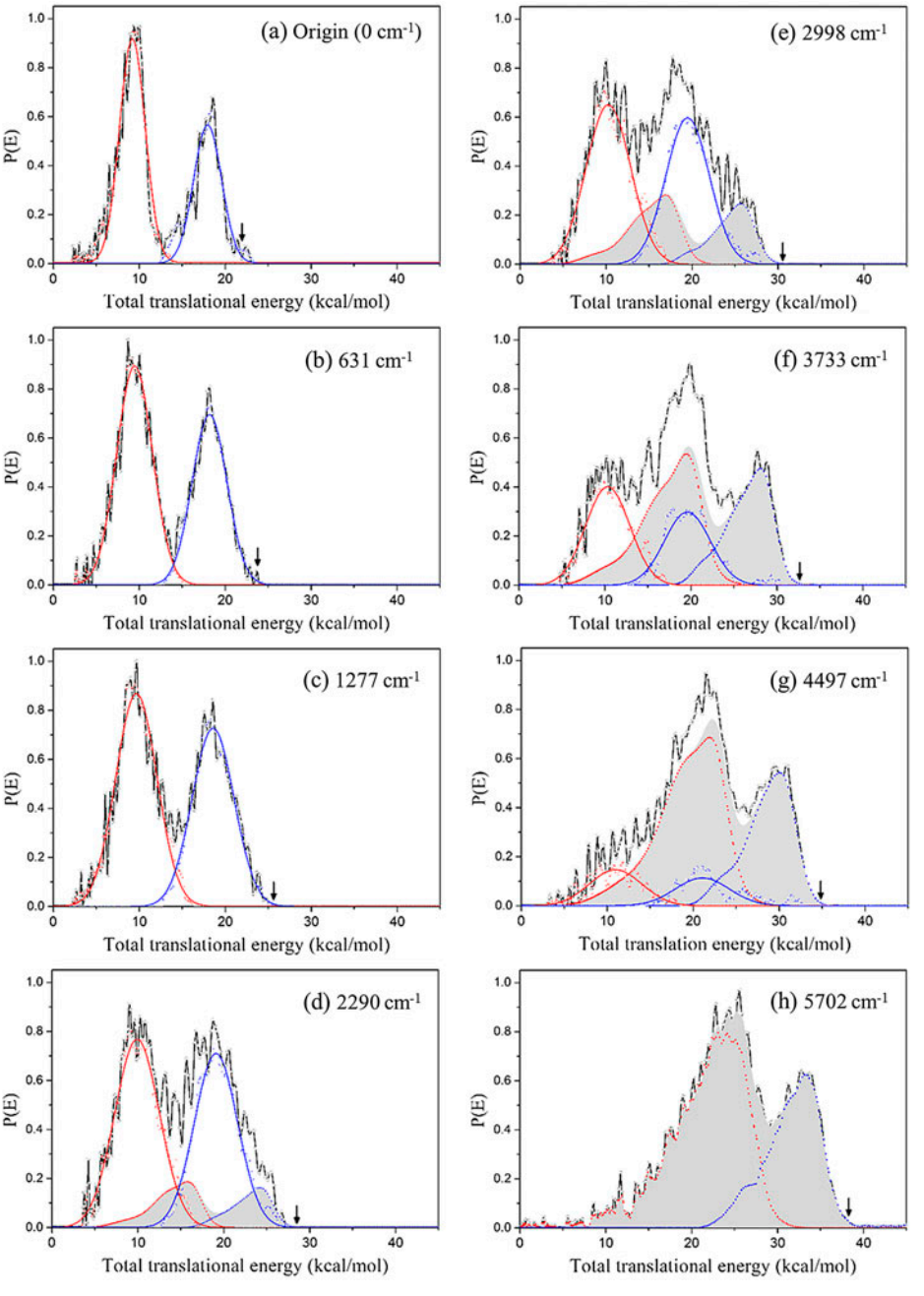

Figure 3. (Colour online) (a)–(h) Total translational energy distributions of the nascent D fragment after subtraction of background signal due to probe laser only at various excitation energies. Photolysis energies minus the S_1 origin of 34,990 cm^{-1} are depicted for each translational energy distribution. The product state distributions associated with the $\tilde{X}$(blue) and $\tilde{A}$(red) states of $C_6H_5S^{\bullet}$ are deconvoluted from the experiment (open circles). Contributions from $S_1 \leftarrow S_0$ excitation (solid lines) and $S_2 \leftarrow S_0$ vertical excitation (shaded) are also deconvoluted from the experimental results. Black arrows indicate the maximum available energies for an S–D bond dissociation energy of 27,308 cm^{-1}.

represents the nonadiabatic channel giving the $C_6H_5S\cdot(\widetilde{X}^2B_1)$ fragment, whereas a distribution with a smaller translational energy is ascribed to the adiabatic channel producing $C_6H_5S\cdot(\widetilde{A}^2B_2)$. Estimation of the branching ratio of $C_6H_5S\cdot(\widetilde{X}^2B_1)$ with respect to $C_6H_5S\cdot(\widetilde{A}^2B_2)$ is then quite straightforward. The branching ratio is estimated to be ~0.75 ± 0.15 at the S_1 origin and remains more or less constant over the energy range of 0–2000 cm^{-1} above the origin [134]. This constant branching ratio over the wide internal energy of S_1 results from the ultrafast S–D bond rupture of the S_1 thiophenol-d_1, indicating that the internal energy given to the initial reactive flux on S_1 does not flow into nuclear motions influencing the S_1/S_2 vibronic coupling strength, as the S–D bond breakage takes place before any energy randomization process occurs.

Interestingly, however, the product angular distribution shows peculiar behaviour as a function of the excitation energy. Since the S–D bond breakage occurs much faster than the molecular rotational period, the D fragment angular distribution should reflect the relative orientation of the transition dipole moment with respect to the laser polarisation axis. The anisotropy parameter (β) is deduced from the relation of $I(\theta) \propto 1 + \beta(E)P_2(\cos\theta)$, where θ is the angle between the pump polarisation and the recoil vector and P_2 is the second order Legendre polynomial [135]. According to the time-dependent density function theory (TDDFT) calculation [136], the $S_1 \leftarrow S_0$ transition dipole moment is parallel to the benzene plane, whereas it is tilted about 20° from the S–D bond axis, as can be seen in Figure 2. The anisotropy parameter (β) is then expected to be positive for the angular distribution of D from the S_1 state of thiophenol. Consistently, β is indeed estimated to be ~0.25 at the S_1 origin band. Strikingly, however, it is found that the anisotropy parameter deceases very sharply with increase of the S_1 internal energy to give the negative β value of −0.60 before going back to nearly zero again, giving a broad peak ($\Delta E \sim 200$ cm^{-1}) in β centred at the S_1 internal energy of ~600 cm^{-1}, as can be seen in Figure 2. This sharp variation of β in the narrow energy region is not explicable without invoking the $S_2 \leftarrow S_0$ excitation, of which the transition dipole moment is perpendicular to both the benzene plane and the S–D bond axis. Since $S_2 \leftarrow S_0$ vertical excitation starts at ~2000 cm^{-1} above the S_1 origin (*vide infra*), however, coherent excitation of S_1 and S_2 is only plausible when the S_1/S_2 conical intersection is accessed by the particular S_1 vibronic band at ~600 cm^{-1}. This vibronic band is most likely attributed to the ν_β normal mode associated with SD in-plane bending motion. There are 33 normal modes for thiophenol, and projection of multi-dimensional potential energy surfaces on each normal mode coordinate will produce 33 different potential energy curves. Obviously, not all of these curves produce surface crossing points [134]. In this regard, it is interesting to find that the S_1 and S_2 surfaces theoretically become degenerate along the ν_β normal mode coordinate. The S_1/S_2 conical intersection point along the ν_β normal mode coordinate (CI^β) then lies on the same conical intersection seam as the minimum energy conical intersection (MECI) which has been theoretically calculated using the CASSCF method. Actually, CI^β and MECI are smoothly connected on the same branching plane without a barrier to generate a conical intersection seam [134]. The bandwidth of the β-dip is similar to that of the PHOFEX vibronic band within the error limit. The simple potential energy curve, drawn as a function of the S–D bond elongation coordinate, gives the S_1/S_2 crossing point at ~1802 cm^{-1} above the minimum energy level of S_1 according to the CASPT2 calculation [115]. Considering the ZPE difference between S_1 and S_2 with respect to the S–D stretching mode, the S_1/S_2 curve crossing is calculated to be ~850 cm^{-1} above the S_1 ZPE level. This somewhat low barrier to the S_1/S_2 curve crossing explains the prompt S–D bond rupture dynamics well.

Starting at ~2000 cm^{-1} above the S_1 origin, the product translational energy distribution shows a sharp shoulder in the high energy region, indicating that a new dynamic channel starts to open at around this energy, as shown in Figure 3. This feature becomes more pronounced at ~3000 cm^{-1} above the origin, giving a third peak representing the $C_6H_5S\bullet(\tilde{X})$ fragment produced from the new channel. As the energy increases, the Gaussian-shaped product state distribution from the S_1 channel diminishes, whereas the product state distribution, which has a higher translational partitioning ratio, becomes dominant. This experimental fact indicates that the new channel is due to the vertical excitation to the high-lying repulsive S_2 state as the direct dissociation naturally gives more translational energy to the fragments. The negative anisotropy parameter of -0.73 ± 0.05, measured at ~4900 and ~5700 cm^{-1} above the S_1 origin, is also consistent with the direction of the S_2–S_0 transition dipole moment which is perpendicular to the molecular plane on which the S–D bond axis is placed. The distinctly different dynamics of the two channels allow the deconvolution of the total translational energy distribution of the nascent fragments into individual contributions from the S_1–S_0 and S_2–S_0 transitions. Intriguingly, the increase of the S_2–S_0 vertical-transition component with increasing excitation energy is quite well correlated with the decrease of the anisotropy parameter of the product angular distribution [134].

In summary, it has been found that the S–H(D) bond dissociation on the S_1/S_2 excited states of thiophenol (-d_1) takes place promptly within the single oscillation period. The S–H(D) bond axis lies on the benzene plane of thiophenol (-d_1) in the ground state, and its planar structure is maintained in the S_1/S_2 optical excitation. Nonadiabatic transition probability is thus found to be quite significant as the conical intersection acting as a dynamic funnel for nonadiabatic transition is generated at the planar branching plane. Most intriguingly, direct access to the nuclear configuration near the conical intersection seam of thiophenol has been manifested by the resonance-like feature in the product angular distribution observed at the specific vibronic band corresponding to the SD in-plane bending mode, unravelling the nature of the complicated nonadiabatic surface crossing structures and the dynamics of the multi-dimensional polyatomic system.

3.2. *Chemical derivatives of thiophenol: conformational manipulation of the nonadiabatic transition probability*

As mentioned above, thiophenol adopts a planar geometry at both ground (S_0) and excited (S_1, S_2) states [112,137], and it is interesting to note that the nuclear configurations along the conical intersection seam for both S_1/S_2 and S_0/S_2 crossings have a plane of symmetry [69,70,112,113,115,134]. The nonadiabatic transition probability at the conical intersection, therefore, should be intimately related to the molecular planarity of the reactive flux. For thiophenol, the S-H bond dissociation is prompt and it occurs on the molecular plane with a significant nonadiabatic transition probability (*vide supra*) as the reactive flux (or wavepacket) with a plane of symmetry would funnel through the conical intersection more efficiently [134]. A naturally arising question would be then whether or not one can manipulate the nonadiabatic transition probability by tuning the molecular planarity of the reactive flux. One straightforward and yet difficult solution could be the use of the IR + UV double resonance technique [54]. Namely, by exploiting the specific property of IR + UV double resonance, the Franck-Condon overlap between the ground and excited states can be modified so that the nuclear configuration of the reactive flux, which is otherwise difficult to access, can be more freely explored. One of the most difficult obstacles in this endeavour, however,

is the molecular size of thiophenol. As the number of internal degrees of freedom is 33, IVR [138] is expected to be significant even at the fundamental vibrational level of the ground electronic state. Particularly, out-of-plane modes, which are expected to be critical in determining the nonadiabatic transition probability [81,88,112], would be hardly accessible in terms of both symmetry and availability of the infrared light source.

In order to modify the molecular planarity of the molecular photodissociation event, we have recently investigated several chemical derivatives of thiophenol [70]. Interestingly, the conformational preference in the ground electronic state is found to be quite different for various chemical substituents at the *para* position of thiophenol. For instance, in 4-methoxythiophenol-d_1, in which the methoxy group is substituted at the *para* position of thiophenol, the C_2C_1SD dihedral angle of the S_0 minimum energy structure is theoretically predicted to be 73° according to our DFT calculation [114,139], as can be seen in Figure 4. Direct excitation of 4-methoxythiophenol-d_1 to the repulsive S_2 state at 243 nm would then prepare the initial reactive flux at the non-planar geometry. In the time-dependent view, as the S_2 minimum energy state adopts the planar geometry, the initial wavepacket is going to be located at the edge of the downhill potential along the C_2C_1SD dihedral angle. Therefore, as the wavepacket moves out along the repulsive S–D coordinate, there will be a strong torque exerted along the C_2C_1SD dihedral angle. This means that the wavepacket will spread out not

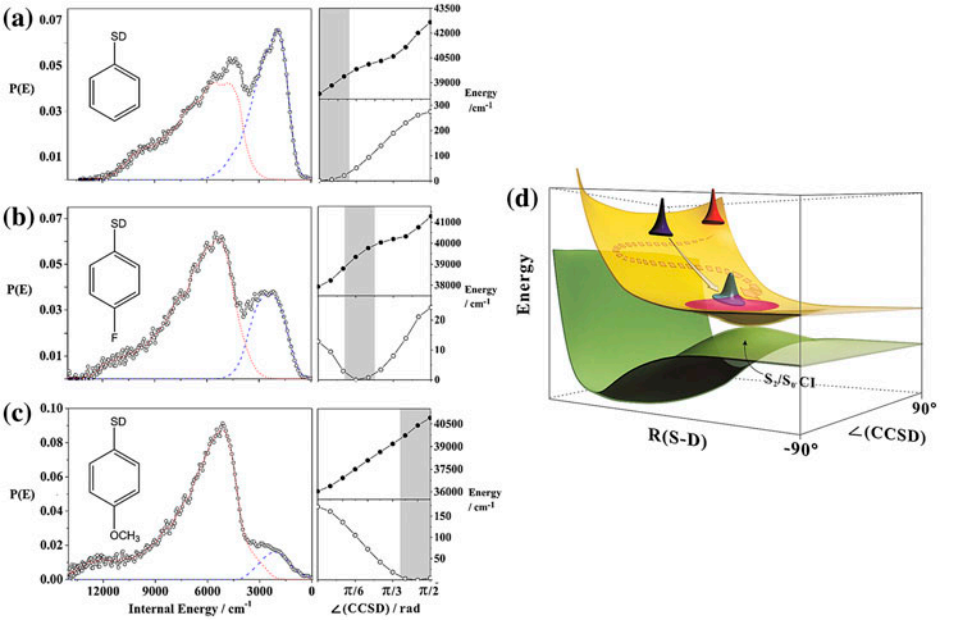

Figure 4. (Colour online) Internal energy distributions (○) of X–C_6H_4–S and the deconvoluted $\tilde{X}$ (—) and $\tilde{A}$ states (•••) deduced from corresponding D images taken at 243 nm for (a) X = H, (b) X = F, and (c) X = OCH_3. On the right, potential energy curves along the CCSD dihedral angle are shown for the ground (○) and S_2 (●) states. Franck-Condon regions are shaded. (d) A simple wavepacket propagation model on two-dimensional PESs. The S_2/S_0 conical intersection is formed at the planar geometry. As the initial location of the optically prepared wavepacket is changed, the bifurcation dynamics on CI is expected to be strongly dependent on the two-dimensional wavepacket spreads. Source: Adapted with permission from Ref. [70]. Copyright (2008) Wiley-VCH Verlag GmbH & Co. KGaA, Weinheim.

only along the dissociating S–D bond but also along the C_2C_1SD angle as the reaction proceeds. This wide spread of the wavepacket at the S_0/S_2 conical intersection along the out-of-plane C_2C_1SD dihedral angle coordinate is then expected to diminish the nonadiabatic transition probability significantly. Indeed, the experiment shows a dramatic decrease of the nonadiabatic channel yield for 4-methoxythiophenol-d_1 compared to that of thiophenol. The $\widetilde{X}/\widetilde{A}$ ratio, the product branching ratio of $C_6H_5S\cdot(\widetilde{X}^2B_1)$ with respect to $C_6H_5S\cdot(\widetilde{A}^2B_2)$, is found to be ~0.1 for 4-methoxythiophenol-d_1, and this is much smaller than the value of 0.75 that is observed for thiophenol at the same pump wavelength of 243 nm [69], as can be seen in Figure 4. This conformational manipulation of the nonadiabatic transition probability has also been demonstrated for 4-fluorothiophenol-d_1 which adopts the minimum energy geometry at the C_2C_1SD angle of 31° [114]. In 4-fluorothiophenol-d_1, the nonadiabatic passage of the wavepacket through the S_0/S_2 conical intersection is expected to be less probable than it is in the case of thiophenol, whereas it will be more probable than it is in the 4-methoxythiophenol case. This is because the extent of the wavepacket spread along the C_2C_1SD dihedral angle in the vicinity of the conical intersection of 4-fluorothiophenol-d_1 lies between those of thiophenol and 4-methoxythiophenol-d_1. As expected, the $\widetilde{X}/\widetilde{A}$ product branching ratio of 4-fluorothiophenol-d_1 at 243 nm is found to be ~0.35, which is consistent with our simple wavepacket model on the two-dimensional potential energy surface. High-level theoretical calculations by Domcke and colleagues [81,112] confirmed our simple wavepacket model that moves on two-dimensional potential surfaces near the conical intersection. Control of the nonadiabatic transition probability by selecting the specific conformational structure has been demonstrated in the photodissociation reactions of thiophenol derivatives [70]. From these experiments, it is possible to establish not only the relationship between the molecular structure and the chemical reactivity but also to find a way to control the reaction outcome by selective preparation of the reactant flux at particular nuclear configurations.

3.3. *Spectroscopic characterisation of conical intersection in the photodissociation of thioanisole*

For thiophenol, the initial quantum states of the reactant molecule are difficult to identify spectroscopically due to their intrinsic ultrashort lifetimes even at the zero-point level of S_1 [113,134]. In order to slow down the photodissociation reaction, we have investigated the photodissociation dynamics of thioanisole ($C_6H_5SCH_3$) [66]. Importantly, the reaction channels of thioanisole at the asymptotic level are exactly the same as those of thiophenol [118,119]. According to CASPT2 calculations, potential energy surfaces along the S–CH_3 bond dissociation coordinate of thioanisole are very similar, in general, to the potential energy surfaces along the S–H bond elongation coordinate of thiophenol. Namely, similar to that of thiophenol, the bound $\pi\pi^*(S_1)$ state of thioanisole is coupled to the repulsive $\pi\sigma^*(S_2)$ state through the first S_1/S_2 conical intersection [47,66]. The ground S_0 state diabatically correlates to the $C_6H_5S\cdot(\widetilde{A}^2B_2)$ product, whereas S_2 leads to $C_6H_5S\cdot(\widetilde{X}^2B_1)$ nonadiabatically, giving the second S_0/S_2 conical intersection at the planar geometry. Now, because of the heavy mass of the methyl moiety, quantum tunnelling through the barrier is much slowed down. Therefore, the S_1 vibronic states of thioanisole are long-lived, and give well-resolved peaks in the resonance two-photon ionisation (R2PI) spectrum [140], as can be seen in Figure 5. Actually, the S_1 state lifetime of thioanisole has recently been measured to be ~1.4 ns at S_1 ($\upsilon = 0$) by Stavros and colleagues [47].

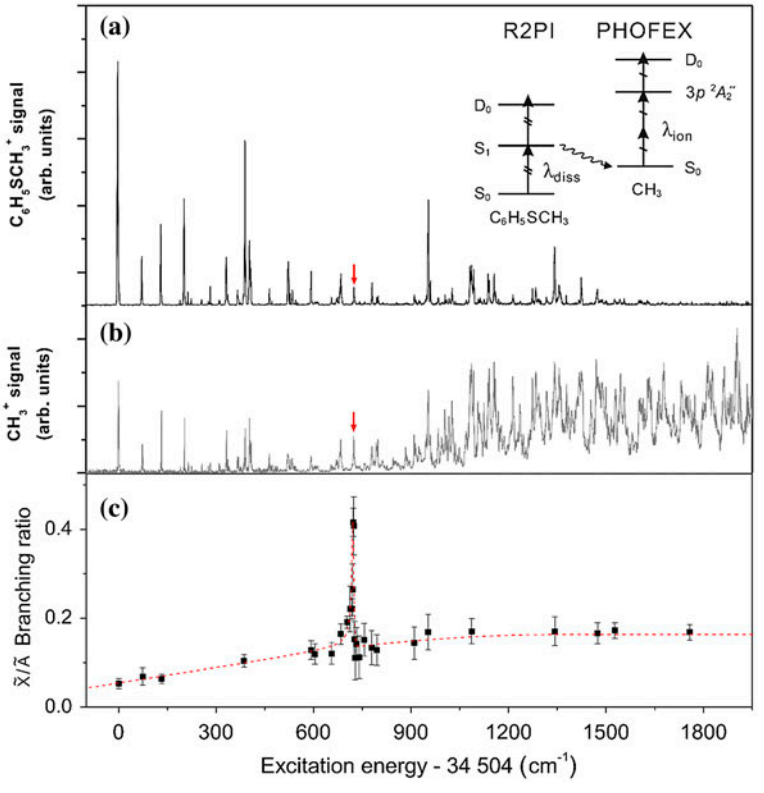

Figure 5. (Colour online) S_1 vibronic levels, total $CH_3{\cdot}(v = 0)$ fragment yield, and $\widetilde{X}/\widetilde{A}$ branching ratio plotted as a function of photoexcitation energy. (a) R2PI spectrum of jet-cooled thioanisole. (b) PHOFEX spectrum monitoring $CH_3{\cdot}(v = 0)$ versus pump energy. The nascent $CH_3{\cdot}$ fragment ($v = 0$) was probed by (2 + 1) ionisation with a laser pulse ($\Delta t \sim 5$ ns) at 333.45 nm using the Q transition via $3p\ ^2A_2''$ without rotational selection. (c) The $\widetilde{X}/\widetilde{A}$ branching ratio shows a sharp resonance feature at an internal energy of 722 cm^{-1}. The dotted line is drawn as a visual aid to show the asymmetric line shape of the branching ratio. Source: Reprinted from Ref. [66].

Interestingly, it has been found that the R2PI spectrum of S_1 thioanisole is quite different from the PHOFEX spectrum which was obtained by monitoring the nascent $\cdot CH_3$ ($v = 0$) fragment as a function of the excitation energy. If the quantum yield for S–CH_3 fragmentation remains constant, PHOFEX is expected to represent the energy-dependent absorption cross section for the S_1–S_0 transition of thioanisole. Actually, the R2PI and PHOFEX spectra show almost identical patterns until the excitation energy reaches the S_1 internal energy region between 700 and 800 cm^{-1}. Above this energy region, the R2PI signal intensity decreases, whereas the PHOFEX signal persists with an emerging broad background, as can be seen in Figure 5. These results indicate that several dynamic constraints may be altered in this energy region. One possibility is that the S_1 state lifetime gets shortened as the pump energy increases, leading to a weaker R2PI signal compared to the PHOFEX signal because of the relatively long temporal window (~5 ns) in the ionisation detection of the parent molecule in the former. Another and yet related possible scenario is that vibronic coupling of the S_1 vibronic states to the S_2 continuum state becomes severe in this energy region. In this case, the

ionisation cross section would be largely modified to give possibly a much reduced R2PI signal, whereas the PHOFEX spectrum would have a complicated energy coupling process. In order to clarify the mechanism behind this huge difference between the case of R2PI and PHOFEX, we have measured the translational energy distribution of the nascent CH_3 fragment at each discernible vibronic band [66].

The total translational energy distributions of $CH_3{\cdot}(v = 0)$ are determined using the velocity-map ion imaging method [141] at different excitation energies corresponding to many distinct S_1 vibronic bands. The upper limit for the S–CH_3 bond energy (D_0) of thioanisole is estimated to be 70.8 ± 0.8 kcal/mol [142]. In the translational energy distribution, the major peak at $E_t \sim 15.6$ kcal/mol is associated with the $C_6H_5S{\cdot}(\widetilde{A}^2B_2)$ + $CH_3{\cdot}(v = 0)$ channel, while the relatively small peak at ~25 kcal/mol represents the $C_6H_5S{\cdot}(\widetilde{X}^2B_1)$ + $CH_3{\cdot}(v = 0)$ channel [66]. For most S_1 vibronic bands, the nonadiabatic reaction leading to the $C_6H_5S{\cdot}(\widetilde{X}^2B_1)$ product is found to be a minor channel, suggesting that the S–CH_3 bond dissociation of S_1 thioanisole mostly follows the adiabatic reaction path to give $C_6H_5S{\cdot}(\widetilde{A}^2B_2)$ at the asymptotic level. For example, the $\widetilde{X}/\widetilde{A}$ product branching ratio is estimated to be ~0.053 at the S_1 origin. This indicates that the nonadiabatic transition probability at the S_0/S_2 conical intersection is very low. This is in contrast to the case of thiophenol [72]. As mentioned above, the S–H(D) bond dissociation of thiophenol occurs promptly with the maintaining of the molecular planarity, therefore showing significant probability for the nonadiabatic transition at the S_0/S_2 conical intersection. In thioanisole, however, the S–CH_3 bond dissociation rate is greatly slowed down and the initially prepared S_1 reactive flux must explore many different nuclear configurations before it is coupled to the repulsive $\pi\sigma^*(S_2)$ state. This time consuming exploration step, which takes place prior to the bond cleavage, causes the reaction to follow the adiabatic pathway all the way to the final products.

In the energy range of 0–2000 cm^{-1} above the S_1 origin of thioanisole, the $\widetilde{X}/\widetilde{A}$ branching ratio remains quite low, indicating that the adiabatic channel is still dominant in this energy range. The $\widetilde{X}/\widetilde{A}$ branching ratio shows a gradual but slow increase to give ~0.15 at E_{int} = 2000 cm^{-1}. Most strikingly, however, we have found that the $\widetilde{X}/\widetilde{A}$ branching ratio shows a very sharp peak value of ~0.45 at the S_1 internal energy of 722 cm^{-1}, as can be seen in Figure 5. This dynamic resonance is hardly explicable at first glance. One tends to think that the initial reactive flux prepared by the optical excitation undergoes full or partial IVR to search for the minimum energy reaction path in the nuclear configuration space. This '*adiabatic*' picture is particularly suitable for most chemical reactions of long-lived excited states. In this picture, initial memory of the excited state in terms of the nuclear configuration is washed out in the course of the exploration of the reactive flux toward the most efficient reaction pathway. Therefore, the dynamic resonance in the product branching ratio observed at the particular S_1 vibronic band of thioanisole is quite rare and very surprising.

In order to characterise the 722 cm^{-1} band of S_1, (1 + 1′) MATI spectroscopy has been employed [66]. In MATI, the first photon is fixed at a specific S_1–S_0 transition and the wavelength of the second photon is varied to probe the vibrational states of the thioanisole cation (D_0) in a pulsed-field ionisation condition [143]. In the MATI spectrum taken via the 722 cm^{-1} band of S_1, according to the propensity rule ($\Delta v = 0$) in the D_0–S_1 ionisation process, the cationic D_0 vibrational mode, of which the nuclear displacement vectors are similar to those of the S_1 intermediate state, is found to be strongly enhanced. The corresponding D_0 vibrational frequency is 743 cm^{-1}, and this matches well with the theoretically predicted value of 733 cm^{-1} for the 7a vibrational mode of the thioanisole cation. The 7a mode is associated with C_1–S–CH_3 asymmetric

stretching motion. The dramatic change of the $\widetilde{X}/\widetilde{A}$ product branching ratio at 722 cm^{-1} then indicates that the nuclear configuration spanned by the 7a vibrational mode excitation should lead to more efficient nonadiabatic transition at the S_0/S_2 conical intersection, giving an enhanced yield of $C_6H_5S\cdot(\widetilde{X}^2B_1)$. As the nuclear configurations spanned by the 7a mode are on the optically bright S_1 state and possibly the close-lying S_2 state, the dynamic resonance observed at 722 cm^{-1} should result from the energy/mode dependent change of the nonadiabatic coupling strength near the S_1/S_2 conical intersection. Most likely, the 7a mode excitation prepares the initial reactant flux in the proximity of the S_1/S_2 conical intersection seam. As the reactive flux on S_2 proceeds very fast along the dissociating S–C elongation coordinate, nuclear configurations of the reactive flux perpendicular to the reaction coordinate at the S_0/S_2 conical intersection are expected to be little changed from those at the first S_1/S_2 conical intersection. This is why the direct access to the S_1/S_2 conical intersection by the 7a mode (S_1) excitation may lead to higher nonadiabatic transition probability, giving the resonance-like increase of the $\widetilde{X}/\widetilde{A}$ product branching ratio. It should be noted that the translational partitioning ratio also slightly increases at the 722 cm^{-1} mode excitation [66]. At the dynamic resonance at 722 cm^{-1}, the small portion of the reactive flux is directly prepared on S_2 at the S_1/S_2 conical intersection, leading to larger translational energies for departing fragments compared to those of the other portion of the reactive flux on S_1. This is because the reactive flux on S_1 explores many different nuclear configurations before it couples to the repulsive S_2, giving more significant excitation of vibrational modes perpendicular to the reaction coordinate. The experimental fact that $C_6H_5S\cdot(\widetilde{A}^2B_2)$ is the major product off the dynamic resonance reflects the fact that the reactive flux on S_2, if prepared indirectly through vibronic coupling via the optically active S_1 state, prefers to follow the adiabatic path at the S_0/S_2 conical intersection.

In order to verify the concept of direct nuclear configurational access to the conical intersection as the origin of the dynamic resonance, the structure of the MECI was theoretically calculated by CASSCF [144,145] and compared with the nuclear configuration spanned by the 7a mode excitation of S_1. Interestingly, it has been found that the nuclear configuration at classical turning points of the 7a mode fundamental excitation along certain critical molecular parameters such as the S–CH_3 bond length is very close to that of MECI [66]. As the conical intersection volume is nonzero as far as the nonadiabatic transition probability is concerned, the nuclear configuration spanned by the 7a mode does not have to be identical to that of MECI to explain the experimentally observed dynamic resonance. Rather, it seems to be more reasonable to state that the 7a mode excitation of S_1 makes direct access of the initial reactive flux to the nuclear configuration possible in the proximity of the S_1/S_2 conical intersection. Our *ab initio* calculations support this idea very well. Overall, despite a number of frequency- and time-resolved experimental studies to date, no molecular-level characterisation of the conical intersection has yet been realised. Our observation of a dynamic resonance in the nonadiabatic transition probability by direct access to the conical intersection region provides the first cornerstone for the spectroscopic characterisation of the conical intersection in the photodissociation reaction.

3.4. *Refining the conical intersection seam and observation of bound resonances embedded in the continuum*

Since it was found that the conical intersection could be spectroscopically probed by analysing product state distributions from the state-selective thioanisole molecule, a

naturally arising next question is whether or not one can refine the multi-dimensional conical intersection seam in the extended internal degrees of freedom. Isotopic substitution would provide an ideal system in this regard as the electronic configurations involved in the optical transition and chemical reactions are expected to be little influenced by isotopic substitution, whereas the nuclear displacement vectors associated with each normal mode will be slightly modified according to the changes of mass-weighted coordinates. Accordingly, we recently have carried out a study of the photodissociation dynamics of thioanisole-d_3 ($C_6H_5S–CD_3$). The R2PI spectrum shows well-resolved S_1 vibronic structures of $C_6H_5SCD_3$ up to ~1100 cm^{-1} above the S_1 origin, as can be seen in Figure 6. On the other hand, the R2PI signal diminishes and completely disappears from ~1500 cm^{-1} above the origin. However, in the PHOFEX spectrum in which the nascent $CD_3\cdot$ fragment yield is monitored as a function of the S_1–S_0 excitation energy, the intensity pattern shows the opposite behaviour. Namely, the $CD_3\cdot$ fragment yield starts to increase at ~1100 cm^{-1} above the origin, showing intense and complicated spectral features in the higher energy region where the R2PI signal is practically absent. These spectral patterns are very similar to those in the case of $C_6H_5SCH_3$ [66], indicating that there should also exist a critical point in this energy region where the dissociation mechanism dramatically changes. The translational energy of the nascent $CD_3\cdot(v = 0)$ fragment was measured at each S_1 vibronic band using the velocity-map ion imaging method [141]. The $\widetilde{X}/\widetilde{A}$ branching ratio was estimated from the relative intensity of the two distinct rings. This ratio is ~0.07 at the S_1 origin and shows a gradual increase with increasing of the S_1 internal energy, giving a value of ~0.15 at the S_1 internal energy of 1500 cm^{-1}. Strikingly, however, and different from the case of thioanisole [66], we have found that the $\widetilde{X}/\widetilde{A}$ branching ratio increases at four distinct S_1 vibronic bands, namely giving sharp peak values of ~0.33 at 656 cm^{-1}, ~0.38 at 705 cm^{-1}, ~0.43 at 708 cm^{-1}, and ~0.20 at 755 cm^{-1}, as can be seen in Figure 6.

Similar to the case of thioanisole [66], in order to unravel the nature of S_1 vibronic bands associated with dynamic resonances, a (1 + 1′) MATI experiment was carried out. Most vibrational bands follow the propensity rule of $\Delta v = 0$, and it was found that the S_1 bands that give dynamic resonances correspond to C_1–S–CD_3 symmetric stretching (ν_s) at 656 cm^{-1}, C_1–S–CD_3 asymmetric stretching (7a) at 705 cm^{-1}, CD_3 wagging ($\beta_{as}CD_3$) at 755 cm^{-1}, and a somewhat mysterious mode at 708 cm^{-1}. In the MATI spectrum taken via the 708 cm^{-1} (S_1) band, three distinct D_0 vibrational bands corresponding to $7a^+$, ($\tau^+ + \nu_s^+$), and $\beta_{as}CD_3^+$ modes are found to be active, where τ^+ is associated with torsion along the dihedral angle between the phenyl moiety and the S–CD_3 bond axis, as can be seen in Figure 7. In the harmonic oscillator approximation [146], the multi-mode character of the 708 cm^{-1} (S_1) band, as manifested in the MATI spectrum, is difficult to explain. Nonetheless, this may indicate that the nuclear configuration accessed by the 708 cm^{-1} band is equivalent to that reached by the combination of C_1–S–CD_3 symmetric stretching, C_1–S–CD_3 asymmetric stretching, and CD_3 wagging modes. Obviously, dynamic resonances corresponding to peak values in the $\widetilde{X}/\widetilde{A}$ branching ratio originate in the more efficient nonadiabatic passage of the reactive flux through the S_0/S_2 conical intersection at resonance frequencies. Direct access to the S_1/S_2 conical intersection at dynamic resonance modes apparently seems to makes less probable the vibrational energy flow into asymmetric coupling modes such as C_2–C_1–S–CD_3 torsion, so that the reactant flux proceeds in the proximity of the S_1/S_2 conical intersection (and therefore also close to the S_0/S_2 conical intersection), resulting in the higher nonadiabatic transition probability, as the reactive flux is less

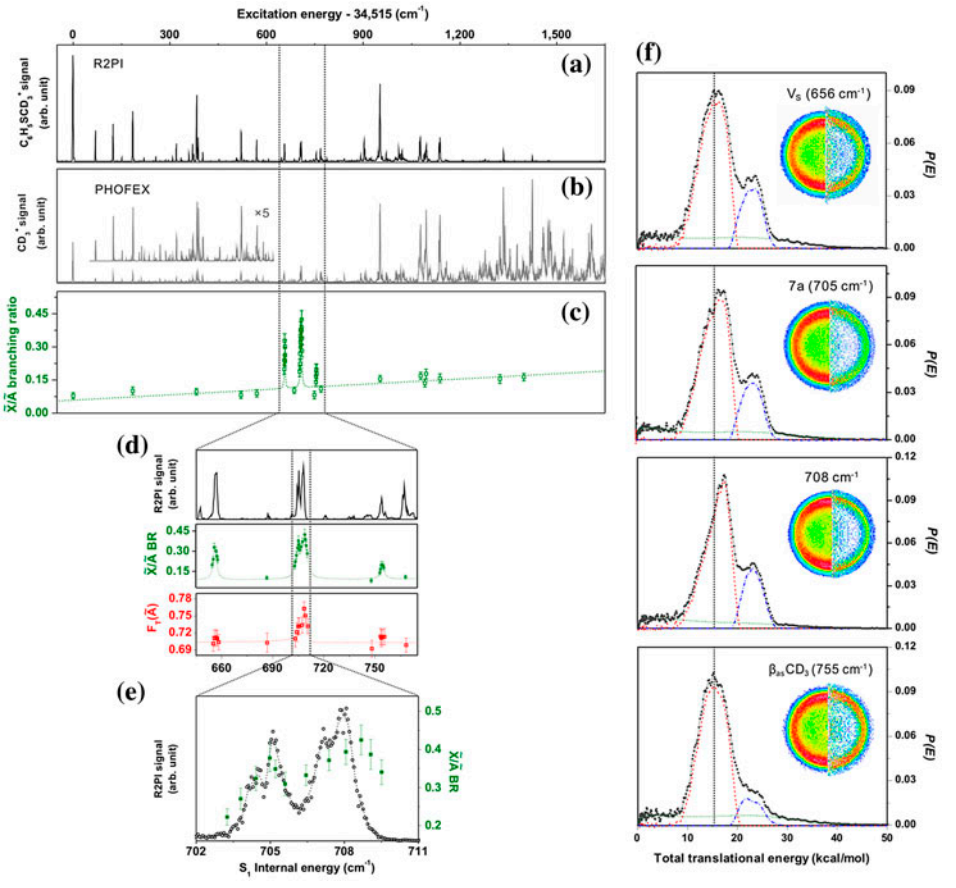

Figure 6. (a) R2PI spectrum of jet-cooled thioanisole-d_3, (b) PHOFEX spectrum taken by monitoring the $\cdot CD_3$ ($v = 0$) fragment yield as a function of excitation energy, (c) the $\widetilde{X}/\widetilde{A}$ branching ratios estimated from the translational distributions of the $\bullet CD_3$ fragment, and (d) enlarged views of the R2PI spectrum, $\widetilde{X}/\widetilde{A}$ branching ratio, and translational energy partitioning ratio for $\widetilde{A}$ ($F_T(\widetilde{A})$). The available energy (E_{avl}) is determined by the relation of $E_{avl} = h\nu - D_0 - \Delta$, where $h\nu$ is the excitation energy, D_0 is the phS–CD_3 bond dissociation energy of 73.5 kcal/mol, and Δ is the energy gap of 8.6 kcal/mol between the $\widetilde{X}$ and $\widetilde{A}$ states of $C_6H_5S\bullet$. (e) Enlarged view of the R2PI spectrum and $\widetilde{X}/\widetilde{A}$ branching ratio around the 708 cm^{-1} region. (f) Total translational energy distributions deduced from CD_3^+ images at S_1 internal energies of 656 (ν_s), 705 (7a), 708, and 755 ($\beta_{as}CD_3$) cm^{-1} bands. Raw (left) and reconstructed (right) images are also shown. The broad background signal shows the quadratic dependence on the pump laser intensity indicating that it is due to two-photon absorption of the parent molecule. The nascent $\bullet CD_3$ radical ($v = 0$) was probed by (2 + 1) ionisation at 333 nm via $3p^2\ A_2''$ state. Source: Reprinted with permission from Ref. [73]. Copyright (2014), AIP Publishing LLC.

dispersed along non-planar degrees of freedom. The experimental fact that the $\widetilde{X}/\widetilde{A}$ product branching ratio shows sharp peak values at four distinct S_1 bands thus indicates that these vibronic excitations bring the initial reactant flux to nuclear configurations near the S_1/S_2 conical intersection seam.

Calculation of full-dimensional potential energy surfaces for this somewhat large molecule with 42 internal degrees of freedom should be a formidable task. Four internal coordinates that are most likely associated with the reaction coordinate are thus

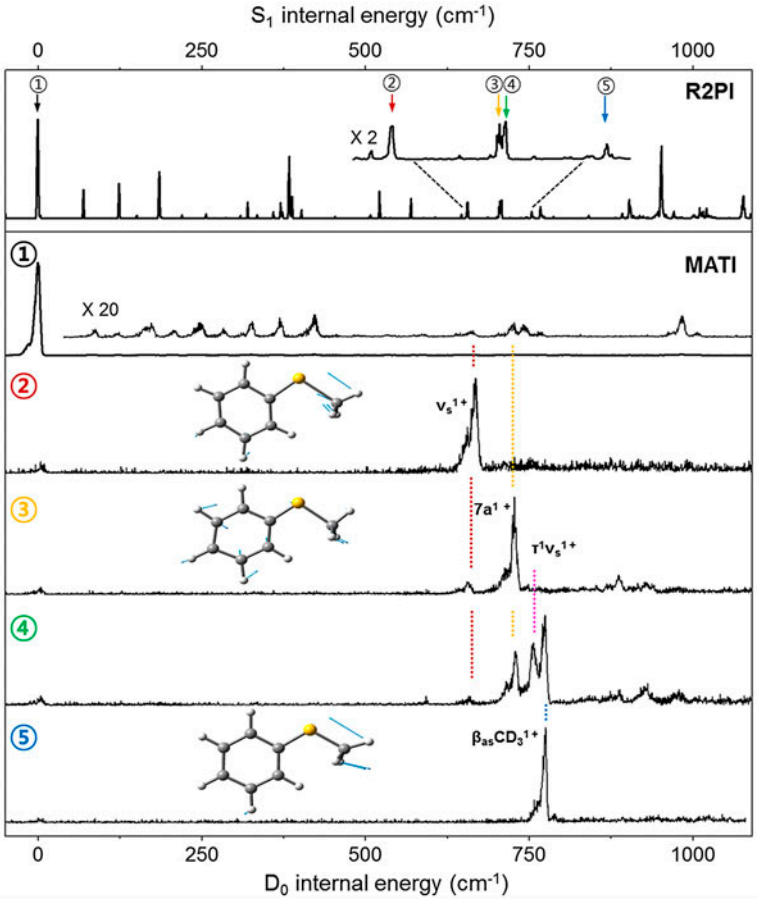

Figure 7. (Colour online) Upper trace: R2PI spectrum of thioanisole-d_3. Lower traces: (1 + 1′) MATI spectra taken via the S_1 origin, 655 (ν_s), 705 (7a), 708, and 755 ($\beta_{as}CD_3$) cm^{-1} bands as intermediate states. Nuclear displacement vector descriptions of corresponding normal modes of D_0 calculated at the B3LYP/6–311++G(3df,3pd) level are shown. Source: Reprinted with permission from Ref. [73]. Copyright (2014), AIP Publishing LLC.

chosen to describe the nuclear configurations near the conical intersection seam, as can be seen in Figure 8. These are d(C–SCD_3), d(CS–CD_3), γ(C–S–CD_3), and γ(S–C–$D_{(3)}$), where the d and γ represent bond length and bending angle, respectively. We carried out *ab initio* calculations (SA4-CASSCF(12,11)/6–311++G(d,p)) to find out the S_1/S_2 conical intersection seam in this reduced dimensionality. The resultant S_1/S_2 conical intersection seam is depicted as a line connecting degenerate points where the difference between the S_1 and S_2 states is calculated to be less than 5 cm^{-1}. Here, the branching plane of the g and h vectors, which are approximately parallel to the S–CD_3 elongation and the C_2–C_1–S–CD_3 dihedral angle coordinates, respectively, provides a platform for the conical intersection seam extended along different nuclear coordinates. In order to visualise how the initial optical transition may access the S_1/S_2 conical intersection region, we examined the nuclear configurations accessed by S_1 vibronic excitations, which are associated with the observed dynamic resonances. Nuclear

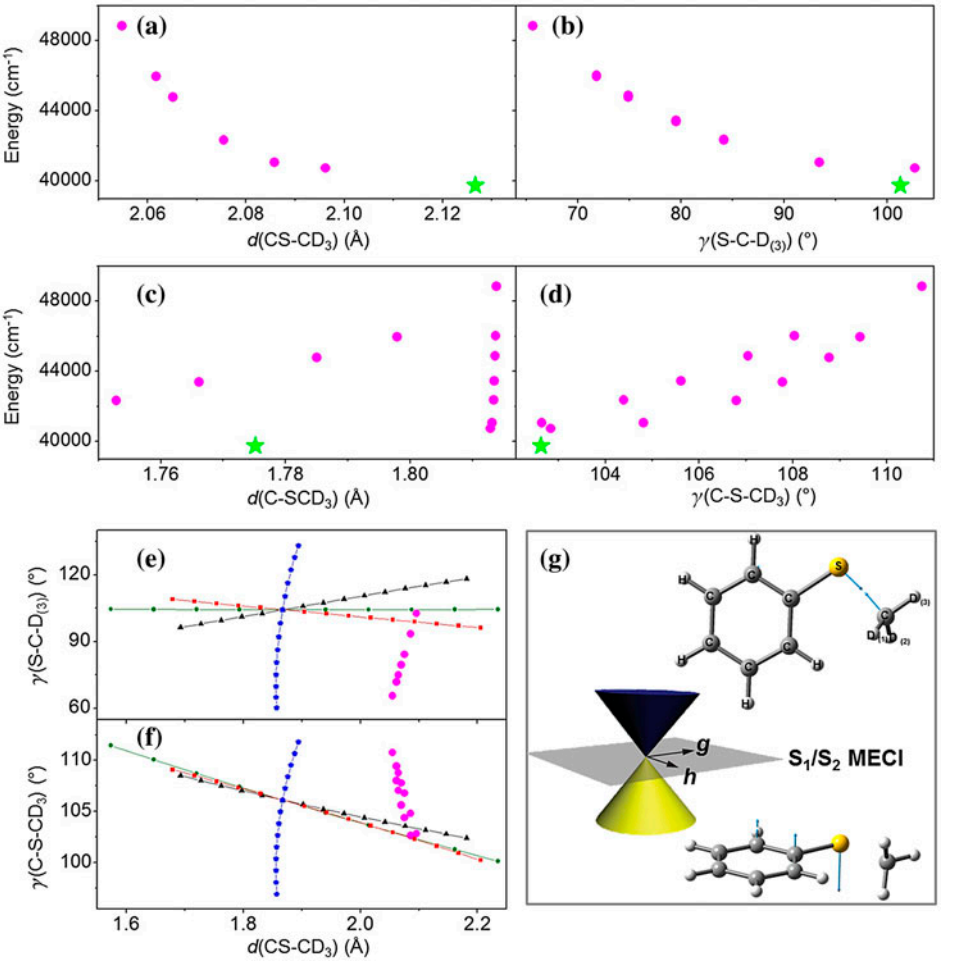

Figure 8. (Colour online) Calculated energies of the conical intersection seam are plotted versus the variation of (a) d(CS–CD_3), (b) γ(S–C–$D_{(3)}$), (c) d(C–SCD_3), or (d) γ(C–S–CD_3). Energy values are relative to the S_0 state. Filled circles (magenta) are electronically degenerate points of S_1 and S_2, whereas the star (green) represents the MECI. Nuclear configurations spanned by the normal mode nuclear displacement vectors are represented as projections onto the (e) d(CS–CD_3)−γ(S–C–$D_{(3)}$) or (f) d(CS–CD_3)−γ(C–S–CD_3) coordinates. Normal mode descriptions for ν_s, 7a, and $\beta_{as}CD_3$ are represented by filled triangles (black line), filled squares (red line), and filled pentagons (blue line), respectively. Filled circles (green line) indicate nuclear configurations which are constructed from the linear combination of displacement vectors of ν_s, 7a, and $\beta_{as}CD_3$ modes at a respective weighting factor of 0.4:0.5:0.1. The gradient difference (g) and nonadiabatic coupling (h) vectors of the branching plane for the conical intersection seam are depicted (g). Source: Reprinted with permission from Ref. [73]. Copyright (2014), AIP Publishing LLC.

displacement vectors of normal modes for the C_1–S–CD_3 symmetric stretching at 656 cm^{-1}, C_1–S–CD_3 asymmetric stretching at 705 cm^{-1}, and CD_3 wagging at 755 cm^{-1} are projected onto the two-dimensional coordinates of d(CS–CD_3) and γ(S–C–$D_{(3)}$) (or d(CS–CD_3) and γ(C–S–CD_3)), as can be seen in Figure 8. Nuclear configurations spanned by the 7a mode are found to partly overlap with those of the conical intersection seam in both projections. Meanwhile, the ν_s mode overlaps with

the conical intersection seam only when its nuclear configuration is projected onto the d(CS–CD_3) and γ(C–S–CD_3) coordinates. This might explain why the 7a mode excitation gives a higher $\widetilde{X}/\widetilde{A}$ branching ratio of ~0.38 compared to the value of ~ 0.33 observed at the ν_s excitation. Namely, as the extent of the overlap of the vibrational wavefunction with the conical intersection seam is larger, the portion of the reactant flux passing in close proximity of the conical intersection seam increases to give the higher nonadiabatic transition probability. On the other hand, the nuclear configurations spanned by the $\beta_{as}CD_3$ mode excitation do not overlap with the conical intersection seam, even though its $\widetilde{X}/\widetilde{A}$ branching ratio of ~0.20 at 755 cm^{-1} is only slightly higher than the average value of ~0.12. This is because in terms of the S–CD_3 bond length the conical intersection seam is not accessible by the $\beta_{as}CD_3$ mode excitation alone within the normal mode description.

The 708 cm^{-1} band that gives the $\widetilde{X}/\widetilde{A}$ branching ratio of ~0.43 has the multi-mode character of C_1–S–CD_3 symmetric stretching, C_1–S–CD_3 asymmetric stretching, and CD_3 wagging modes. Intriguingly, all of these individual modes show dynamic resonances in the $\widetilde{X}/\widetilde{A}$ branching ratio. Thus the 708 cm^{-1} vibrational wavefunction, which can be constructed as a linear combination of ν_s, 7a, and $\beta_{as}CD_3$ modes, could mostly overlap with the conical intersection seam, giving the highest $\widetilde{X}/\widetilde{A}$ branching ratio among the four resonance modes. Energetically, the 708 cm^{-1} band cannot be a combination mode of these S_1 normal modes within the harmonic oscillator approximation. Rather, this band could be a unique S_1 mode for which the nuclear displacement vectors obviously cannot be represented by the single D_0 vibrational mode. In other words, the potential energy surface along this particular mode coordinate may be strongly perturbed by the proximal presence of the S_1/S_2 conical intersection, which may also guide the nonadiabatic path of the reactant flux along the S–CD_3 bond dissociation pathway. This particular vibronic band may then represent *a resonance band embedded in the continuum* generated by the conical intersection, which was predicted long ago by Neumann and Wigner [147] in 1929 and theoretically confirmed later by Cederbaum and colleagues [148,149]. It should be noted that our use of the phrase *a resonance band embedded in the continuum* could confuse readers, as the excited states undergoing predissociation via coupling to the nearby continuum state [150] are often called 'resonances embedded in the continuum'. Here, we would like to narrowly define *a resonance embedded in the continuum* as a quasi-bound state that is generated by a nearby conical intersection. More specifically, the repulsive S_2 state of thioanisole is the continuum state because it is unbound along one particular nuclear coordinate, whereas it is bound with respect to all remaining 41 degrees of freedom at least at the zero-point level. Because of the S_1/S_2 curve crossing, however, the potential energy surface is expected to be strongly perturbed especially with respect to this particular nuclear coordinate along which S_2 is unbound at the conical intersection region. In this case, the adiabatic potential energy surfaces corresponding to the upper cone of the conical intersection actually become bound for all degrees of freedom. Thus, a vibronic state that would otherwise be continuum without the conical intersection becomes a bound state in the perturbed potential energy surfaces. Therefore, one possible scenario is that the 708 cm^{-1} band may represent this particular nuclear coordinate along which the diabatic S_2 is continuum and yet the perturbed potential energy surface is bound in the proximity of the conical intersection. The nuclear displacement vector of the 708 cm^{-1} band, constructed by a linear combination of ν_s, 7a, and $\beta_{as}CD_3$ modes, may then reflect the nuclear motion along the reaction coordinate which is apparently parallel to the g vector of the branching plane. In this sense, the transfer of the S_1

vibrational energy into the translational energy of the departing fragments may occur quite efficiently at the 708 cm^{-1} band, as the corresponding nuclear displacement vector actually points toward the relative translational motion of the departing $C_6H_5S\cdot$ and $CD_3\cdot$ fragments. Intriguingly, this has been clearly manifested in the experimental product kinetic energy distribution. Namely, at the dynamic resonance at 708 cm^{-1}, the translational energy distribution abruptly shifts to the higher energy region, showing a sharp peak when the product translational energy partitioning ratio is plotted versus the excitation energy, as can be seen in Figure 6. A sudden change of the translational energy distribution of products within a tiny energy range is very rare and strongly indicates that the 708 cm^{-1} band represents a nuclear configuration on the conical intersection bearing the multi-dimensional nature of the reaction coordinate.

The overlap of the vibrational wavefunction with the conical intersection seam actually turns out to be extremely sensitive to nuclear displacements associated with each normal mode and energetics involved. In this sense, the reason why the dynamic resonance is not observed at the C_1–S–CH_3 symmetric stretching (ν_s) and CH_3 wagging ($\beta_{as}CH_3$) modes in the $C_6H_5SCH_3$ dissociation may lie in subtle differences of these normal modes in terms of the detailed nuclear displacement vectors in the mass-weighted coordinate. Actually, the ν_s normal mode of $C_6H_5SCH_3$ was calculated to be slightly different from that of $C_6H_5SCD_3$, and the nuclear displacement vector does not access the conical intersection seam in our calculations [73]. Energetically, the $\beta_{as}CH_3$ vibrational energy in $C_6H_5SCH_3$ is quite high, and thus its excitation region should be far from the conical intersection seam. It should be noted that the 722 cm^{-1} band [66] of S_1 $C_6H_5SCH_3$ may represent *a resonance band embedded in the continuum*, judging from the similarity of its mode dynamics to that of the 708 cm^{-1} band of S_1 $C_6H_5SCD_3$, although further experimental and theoretical studies will be required for confirmation. Currently, for the further exploration of the conical intersection seam in the more refined normal mode space, the photodissociation dynamics of partially deuterated thioanisoles such as thioanisole-d_1 ($C_6H_5SCH_2D$) or thioanisole-d_2 ($C_6H_5SCHD_2$) are being investigated. It is intriguing to note that there exist two different conformational isomers for both $C_6H_5SCH_2D$ and $C_6H_5SCHD_2$ with respect to the hindered rotation of the methyl moiety with respect to the rest of the molecule [151]. This provides an opportunity for the systematic investigation of the conformer-selective nonadiabatic dynamics.

Our experimental findings concerning the nuclear configurations responsible for degenerate electronically excited states reveal for the first time the multi-dimensional facets of the conical intersection seam in the chemical reaction of the polyatomic system. It is interesting to note that the nuclear configurations of the initial reactant flux are so critical in the nonadiabatic reaction dynamics occurring on the excited electronic states through strong coupling of nuclear and electronic motions beyond the Born–Oppenheimer approximation [2,3]. Our experimental findings may lead to a more thorough understanding and detailed control of chemical reactions in excited states.

3.5. *IVR and nonadiabatic dynamics in the proximity of the conical intersection*

For polyatomic molecular systems, energy randomization, mainly by IVR, becomes non-negligible very quickly as the density of the states increases exponentially with increasing internal energy [138]. For reactive flux initially prepared on the repulsive excited state, bond breakage occurs much faster than IVR. Thus the nuclear configuration of the initial reactive flux could be critical in the determination of the reaction

pathway. This has already been demonstrated for photodissociation reactions of chemical derivatives of thiophenol on the repulsive S_2 states, and we learned that the conformational preference in the ground state can be used to manipulate the nonadiabatic transition probability (*vide supra*) [70,114]. The S–H(D) bond rupture of thiophenol(-d_1) on S_1/S_2 is ultrafast and IVR does not seem to play a significant role in the photodissociation pathway. For thioanisole, however, the S_1 state lifetime is several hundreds of picoseconds [47,66,73], and thus the dynamic role of IVR in nonadiabatic reaction dynamics should be carefully considered. Actually, MATI and/or SEVI spectroscopic techniques turns out to be extremely useful in the qualitative and/or quantitative analysis of IVR in the S_1 state [132,133]. When IVR is significant at the S_1 intermediate level, the corresponding MATI or SEVI spectrum no longer follows the propensity rule. Instead, the MATI or SEVI signal shows a broad spectral feature, indicating that the associated S_1 intermediate state becomes more or less chaotic. Fortunately, the S_1/S_2 conical intersection of thioanisole is located at the very low internal energy of 600–700 cm^{-1} above the S_1 ZPE level, and IVR is found to be inactive in such a low internal energy region, as manifested in the MATI and/or SEVI spectra, which do follow the propensity rule. This is one of the main reasons why such dramatic dynamic resonances can be clearly observed in the photodissociation reactions of thioanisole [66] and thioanisole-d_3 [73].

When we add a methyl group to the *para*-position of thioanisole, however, it is found that IVR now plays a significant role even at low internal energies of S_1. Namely, in the photodissociation dynamics of *p*-methylthioanisole (*p*-$CH_3C_6H_4SCH_3$), MATI spectra become featureless quite early as the S_1 internal energy increases. Namely, the propensity rule in MATI is maintained only from the S_1 origin up to the 552 cm^{-1} vibronic band. Starting from the 573 cm^{-1} (S_1) band, the MATI spectra become broad and featureless, indicating that IVR plays a significant role, as can be seen in Figure 9. The methyl rotor is a well-known energy randomizer [152,153], and thus the early action of IVR in the S_1 state of *p*-methylthioanisole is not surprising. When IVR is significant, the mode-specificity is expected to be washed out, and therefore it seems unfeasible to find out nuclear configurations associated with the conical intersection seam. Indeed, even though the *para* addition of the methyl moiety to thioanisole is not expected to influence the energetics and structures of the electronic and nuclear configurations along the whole reaction pathway, we were not able to observe a dynamic resonance in the nonadiabatic transition probability in the photodissociation reaction of *p*-methylthioanisole. It is interesting to note that this experimental result in turn supports the idea that the dynamic resonances observed in thioanisole and thioanisole-d_3 originate from direct access of the initial reactant flux to the nuclear configurations in the proximity of the conical intersection [66,73].

The dynamic interplay between IVR and the nonadiabatic transition has also been investigated using 2-fluorothiophenol-d_1 (2-FTP-d_1) and 2-cholorthiophenol-d_1 (2-CTP-d_1) [75]. Velocity-map ion images of D^+ from 2-FTP-d_1 to 2-CTP-d_1 were obtained at excitation energies in the 281–265 and 289–275 nm regions, respectively. In the D fragment translational energy distributions, after the subtraction of the background signal, two distinct Gaussian-shaped distributions were clearly resolved to give the precise $\widetilde{X}/\widetilde{A}$ branching ratio at the given S_1 excitation wavelength [75]. The energy gaps between the two peaks in the translational energy distribution are ~2800 and ~2100 cm^{-1} for the F–C_6H_4S or Cl–C_6H_4S radicals, respectively. These values are consistent with the calculated (CASPT2) [154] values of 2752 and 2148 cm^{-1} for the $\widetilde{A}$–$\widetilde{X}$ vertical energy gap of the F–C_6H_4S or Cl–C_6H_4S radicals, respectively. The $\widetilde{X}/\widetilde{A}$

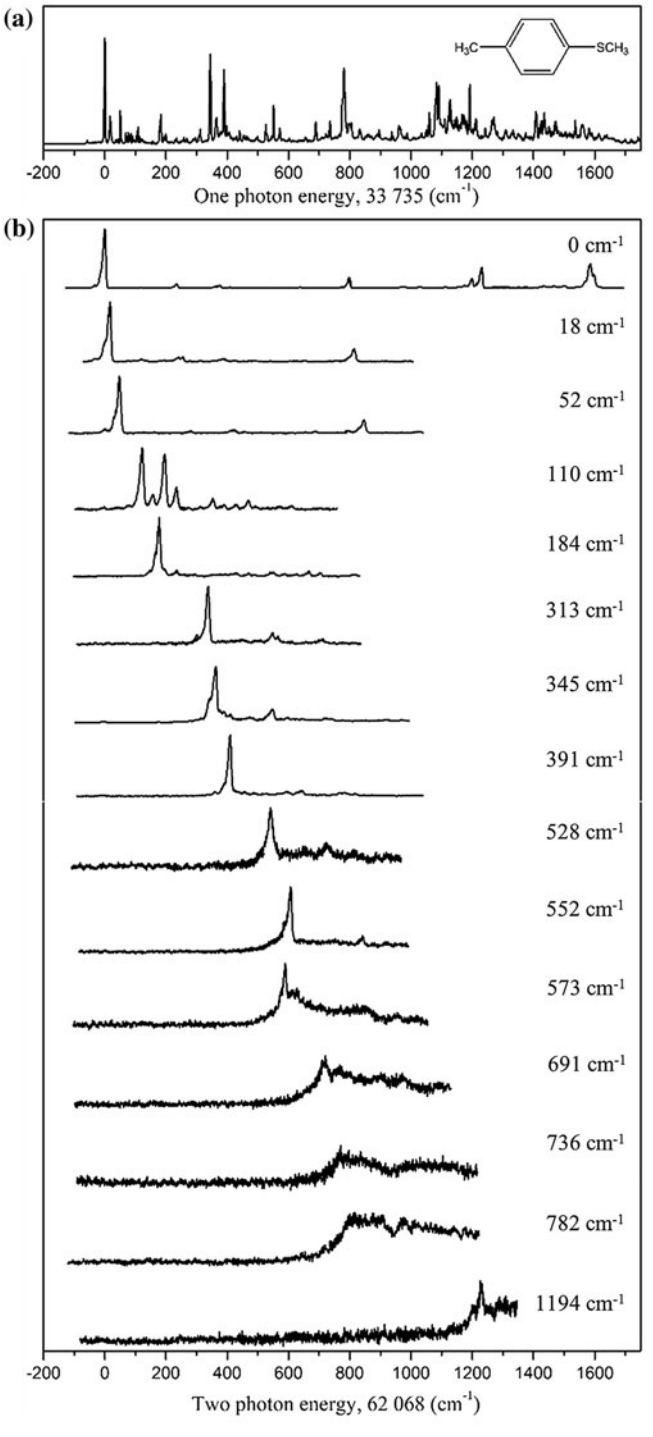

Figure 9. (a) R2PI spectrum of p-methylthioanisole. The origin band is at 33,735 cm^{-1} which is ~770 cm^{-1} lower than that of thioanisole. (b) (1 + 1′) MATI spectra via the origin and several vibronic energies of S_1 state, in which the two photon energy of the origin band is 62,068 cm^{-1}.

product branching ratio representing the nonadiabatic transition probability is then estimated from the relative ratio of two de-convoluted Gaussian-shaped distributions after background subtraction. The $\widetilde{X}/\widetilde{A}$ branching ratio of 2-FTP-d_1 at its S_1 origin is ~1.4, indicating that the nonadiabatic transition probability at the S_0/S_2 conical intersection is quite significant. However, as the S_1 internal energy increases, the $\widetilde{X}/\widetilde{A}$ ratio sharply decreases to ~0.4 at ~1200 cm^{-1} above the S_1 origin and remains constant at higher excitation energies, as can be seen in Figure 10. On the other hand, the $\widetilde{X}/\widetilde{A}$ branching ratio of 2-CTP-d_1 at the S_1 origin is ~1.05, and it is found to be more or less constant up to ~2000 cm^{-1} above the origin. The different behaviours of 2-FTP-d_1 and 2-CTP-d_1 in terms of the nonadiabatic transition probability as a function of the S_1 internal energy are surprising, as the S–D bond dissociation pathways of these two molecules are not expected to be much different.

The sharp decrease of the $\widetilde{X}/\widetilde{A}$ branching ratio observed for 2-FTP-d_1 may then indicate that the reaction path becomes non-planar with increase of the S_1 internal energy. At the S_1 ZPE level, the S–D bond dissociation occurs via tunnelling through the reaction barrier generated by the S_1/S_2 conical intersection. The reactive flux on the repulsive S_2 state then partly undergoes nonadiabatic transition at the S_0/S_2 conical intersection to produce the ground state of the F–C_6H_4S radical. An abrupt decrease of the $\widetilde{X}/\widetilde{A}$ branching ratio to ~ 0.8 (from ~1.4 at the S_1 origin) is observed at the 233 cm^{-1} vibronic band which is associated with C_1SD in-plane bending. This mode may contribute to the weakening of the F•••D intramolecular hydrogen bond, which

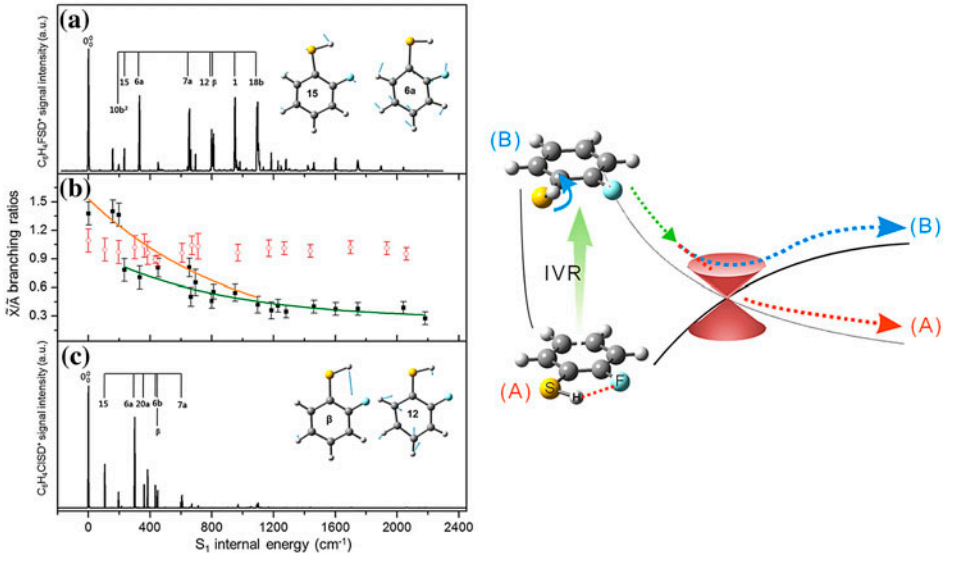

Figure 10. (Colour online) R2PI spectra of (a) 2-fluorothiophenol-d_1 and (c) 2-chlorothiophenol-d_1 with appropriate vibrational mode assignments. The experimentally estimated $\widetilde{X}/\widetilde{A}$ branching ratios are plotted as a function of the S_1 internal energy for 2-fluorothiophenol-d_1 (black filled squares) and 2-chlorothiophenol-d_1 (red open circles) in (b). Nuclear displacement vectors of notable vibrational modes of 2-fluorothiophenol-d_1 are also shown in the inset. Exponential curves are drawn for the visual aid. On the right, a simplified schematic view of the photodissociation reaction of 2-fluoro, chlorothiophenol. The dynamic interplay between the intramolecular hydrogen bonding and IVR is critical in nonadiabatic reaction dynamics. Source: Adapted with permission from Ref. [75]. Copyright (2014) American Chemical Society.

may lead to a decrease of the C_2C_1SD torsional barrier height, which is intrinsically dynamic and thus sensitive to the relevant vibrational activation. As the torsional barrier is lowered, the reactive flux becomes more dispersed along the out-of-plane C_2C_1SD torsional angle. This might make the reactive flux take the tunnelling path through the reaction barrier at the non-planar geometry. The effective barrier for the S–D tunnelling will be adiabatically lowered at the non-planar geometry compared to the case of planar geometry. The nonadiabatic transition probability of the reactive flux tunnelling at the non-planar geometry will be diminished at the S_0/S_2 conical intersection, yielding a smaller $\widetilde{X}/\widetilde{A}$ branching ratio. For other vibronic modes, the $\widetilde{X}/\widetilde{A}$ branching ratio shows a gradual decrease with increase of the S_1 internal energy, yielding a value of ~0.4 at ~1200 cm^{-1} above the origin. This may indicate that the F•••D intramolecular hydrogen bond becomes completely loosened at ~1200 cm^{-1} or higher energies above the origin, resulting in a large probability for the non-planar adiabatic passage of the reactive flux at the S_0/S_2 conical intersection. The opposite behaviour of the $\widetilde{X}/\widetilde{A}$ branching ratio as a function of the S_1 internal energy for 2-CTP-d_1 seems to originate from its Cl•••D intramolecular hydrogen bond, which is stronger than the F•••D intramolecular hydrogen bond of 2-FTP-d_1. Actually, according to the CASPT2 calculation [75], the C_2C_1SD torsional barrier height of 2-CTP-d_1 is predicted to be ~400 cm^{-1} higher than that of 2-FTP-d_1 in the S_1 state. This suggests that the relatively stronger intramolecular hydrogen bonding of 2-CTP-d_1 causes the molecule to retain its molecular planarity even at high internal energy excitation, yielding an $\widetilde{X}/\widetilde{A}$ branching ratio that remains constant up to ~2000 cm^{-1} above the origin. In other words, for 2-FTP, the dissociation path becomes adiabatic as the S_1 internal energy increases, indicating that the reactive flux prefers taking the tunnelling path through the adiabatically lowered reaction barrier at the non-planar geometry with the increase in the internal energy. In 2-CTP, on the other hand, due to the relatively stronger intramolecular hydrogen bonding, the nonadiabatic transition probability remains significant even at high internal energies. These experimental results suggest that the nonadiabatic transition probability can be predicted based on fundamental understanding of the dynamic interplay between vibrational energy flow and molecular structure mediated by the intramolecular hydrogen bonding.

4. Conclusion and perspective

In this article, we have summarised a series of experimental works [66,68–70,72,73,75,134], mainly from our own group, regarding conical intersection dynamics in the photodissociation reaction. Molecular-level understanding of the nonadiabatic dynamics mechanism is essential in explaining a number of important chemical and biological processes in nature. The importance of the conical intersection as a dynamic bottleneck in nonadiabatic chemical reactions has been widely recognised in recent decades. Despite a number of important and successful theoretical and experimental studies to date, however, understanding of the quantum mechanical nature of the conical intersection still remains a difficult challenge. Our recent experimental findings regarding conical intersections provide a cornerstone for spectroscopic characterization of the conical intersection, which is multi-dimensional in nature. For instance, multiple dynamic resonances observed in the photodissociation reaction of thioanisole-d_3 reflect important facets of the multi-dimensional conical intersection seam [73]. The theoretical concept that the nonadiabatic transition probability can be increased when the reactive flux accesses nuclear configurations in the proximity of a conical intersection seam has

now been experimentally demonstrated. Our experimental finding of a *resonance band embedded in the continuum* generated by the conical intersection is also noteworthy. This may be the first experimental observation of such a resonance phenomenon in a photodissociation reaction, though further studies will be required for confirmation. Our experimental results provide an important clue about how one could get the molecular structures and associated dynamic roles of the conical intersection in molecule-specific detail. Full-dimensional quantum-mechanical calculations will be highly desirable for better understanding of nonadiabatic photodissociation dynamics of thiophenols and thioanisoles.

Finding out nuclear configurations in the proximity of a multi-dimensional conical intersection seam is exciting as such a finding could allow for reaction control in specific nonadiabatic chemical processes. For instance, it might be possible to control the nuclear-electronic coupling strength by applying strong external electric or magnetic fields [155,161] in conjunction with spectroscopic characterization of the conical intersection. One would be able to tune the nuclear configuration of the initial reactant flux by utilising different spectroscopic tools such as IR (Raman) + UV double resonances [54] or a stimulated-emission pumping scheme [156]. The application of various spectroscopic techniques will be quite fruitful if one knows the topology and energetics of the conical intersection seam. Using a Stark-deflector [157–160], a specific conformer could be spatially separated from many other conformers populated in the jet, providing the opportunity to investigate conformer-specific nonadiabatic dynamics. As demonstrated previously in the photodissociation dynamics of several chemical derivatives of thiophenol [70,75,114], the conformational structure could be one of the key factors in determining the nonadiabaticity of chemical reactions. Regarding conical intersection dynamics, there remain interesting and important challenges in terms of both theory and experiment. These may include control of nonadiabatic transition probability by state/structure selection or strong external field, full-dimensional description of the conical intersection seam, estimation of the conical intersection volume in terms of its structure and energetics, and quantum-mechanical characterization of resonances embedded in the continuum that are generated by the conical intersection.

Disclosure statement

No potential conflict of interest was reported by the authors.

Funding

This work was supported by the Samsung Science and Technology Foundation under [project number SSTF-BA1401-09].

References

[1] M. Born and R. Oppenheimer, Ann. Phys. **84**, 457 (1927).
[2] G.A. Worth and L.S. Cederbaum, Annu. Rev. Phys. Chem. **55**, 127 (2004).
[3] L.J. Butler, Annu. Rev. Phys. Chem. **49**, 125 (1998).
[4] A.L. Sobolewski, W. Domcke, C. Dedonder-Lardeux, and C. Jouvet, Phys. Chem. Chem. Phys. **4**, 1093 (2002).
[5] M. Barbatti, H. Lischka, S. Salzmann, and C.M. Marian, J. Chem. Phys. **130**, 034305 (2009).

[6] C. Ko, B. Levine, A. Toniolo, L. Manohar, S. Olsen, H.-J. Werner, and T.J. Martínez, J. Am. Chem. Soc. **125**, 12710 (2003).
[7] S. Yamazaki, W. Domcke, and A.L. Sobolewski, J. Phys. Chem. A **112**, 11965 (2008).
[8] H. Kang, K.T. Lee, B. Jung, Y.J. Ko, and S.K. Kim, J. Am. Chem. Soc. **124**, 12958 (2002).
[9] T. Horio, T. Fuji, Y.-I. Suzuki, and T. Suzuki, J. Am. Chem. Soc. **131**, 10392 (2009).
[10] Y.-I. Suzuki, T. Fuji, T. Horio, and T. Suzuki, J. Chem. Phys. **132**, 174302 (2010).
[11] O. Geßner, E.t.H. Chrysostom, A.M.D. Lee, D.M. Wardlaw, M.L. Ho, S.J. Lee, B.M. Cheng, M.Z. Zgierski, I.-C. Chen, J.P. Shaffer, C.C. Hayden, and A. Stolow, Faraday Discuss. **127**, 193 (2004).
[12] J.-W. Ho, H.-C. Yen, W.-K. Chou, C.-N. Weng, L.-H. Cheng, H.-Q. Shi, S.-H. Lai, and P.-Y. Cheng, J. Phys. Chem. A **115,** 8406 (2011).
[13] G. Zgrablić, A.M. Novello, and F. Parmigiani, J. Am. Chem. Soc. **134,** 955 (2012).
[14] X. Zhou, P. Ranitovic, C.W. Hogle, J.H.D. Eland, H.C. Kapteyn, and M.M. Murnane, Nat. Phys. **8,** 232 (2012).
[15] A. Stolow and J.G. Underwood, *Advances in Chemical Physics* (Wiley, Hoboken, NJ, 2008), pp. 497–584.
[16] J.D. Young, M. Staniforth, J.C. Dean, G.M. Roberts, F. Mazzoni, T.N.V. Karsili, M.N.R. Ashfold, T.S. Zwier, and V.G. Stavros, J. Phys. Chem. Lett. **5**, 2138 (2014).
[17] M. Mališ, Y. Loquais, E. Gloaguen, C. Jouvet, V. Brenner, M. Mons, I. Ljubić, and N. Došlić, Phys. Chem. Chem. Phys. **16**, 2285 (2014).
[18] M. Garavelli, P. Celani, F. Bernardi, M.A. Robb, and M. Olivucci, J. Am. Chem. Soc. **119**, 6891 (1997).
[19] D. Polli, O. Weingart, D. Brida, E. Poli, M. Maiuri, K.M. Spillane, A. Bottoni, P. Kukura, R.A. Mathies, G. Cerullo, and M. Garavelli, Angew. Chem. Int. Ed. **53**, 2504 (2014).
[20] D. Asturiol, B. Lasorne, G.A. Worth, M.A. Robb, and L. Blancafort, Phys. Chem. Chem. Phys. **12**, 4949 (2010).
[21] H. Satzger, D. Townsend, M.Z. Zgierski, S. Patchkovskii, S. Ullrich, and A. Stolow, Proc. Nat. Acad. Sci. **103**, 10196 (2006).
[22] S. Ullrich, T. Schultz, M.Z. Zgierski, and A. Stolow, Phys. Chem. Chem. Phys. **6**, 2796 (2004).
[23] O. David, C. Dedonder-Lardeux, and C. Jouvet, Int. Rev. Phys. Chem. **21**, 499 (2002).
[24] B.C. Arruda and R.J. Sension, Phys. Chem. Chem. Phys. **16**, 4439 (2014).
[25] S.A. Trushin, W. Fuß, and W.E. Schmid, Chem. Phys. **259**, 313 (2000).
[26] D.R. Yarkony, Chem. Rev. **112**, 481 (2012).
[27] J.C. Tully, J. Chem. Phys. **137**, 22A301 (2012).
[28] W. Domcke and D.R. Yarkony, Annu. Rev. Phys. Chem. **63**, 325 (2012).
[29] M.J. Rosker, T.S. Rose, and A.H. Zewail, Chem. Phys. Lett. **146**, 175 (1988).
[30] P. Cong, A. Mokhtari, and A.H. Zewail, Chem. Phys. Lett. **172**, 109 (1990).
[31] T.S. Rose, M.J. Rosker, and A.H. Zewail, J. Chem. Phys. **88**, 6672 (1988); J. Chem. Phys. **91**, 7415 (1989).
[32] J.C. Polanyi and A.H. Zewail, Acc. Chem. Res. **28**, 119 (1995).
[33] A. Mokhtari, P. Cong, J.L. Herek, and A.H. Zewail, Nature **348**, 225 (1990).
[34] C. Zener, Proc. R. Soc. London, Ser. A. **137**, 696 (1932).
[35] E. Teller, J. Phys. Chem. **41**, 109 (1937).
[36] D.R. Yarkony, Rev. Mod. Phys. **68**, 985 (1996).
[37] W. Domcke, D.R. Yarkony, and H. Köppel, *Conical Intersections: Electronic Structure, Dynamics and Spectroscopy*, (World Scientific Publishing, Singapore, 2004).
[38] W. Domcke, D.R. Yarkony, and H. Koppel, *Conical Intersections: Theory, Computation and Experiment*, (World Scientific Publishing, Singapore, 2011).
[39] D.R. Yarkony, J. Phys. Chem. A **105**, 6277 (2001).
[40] M.V. Berry, Proc. R. Soc. London, Ser. A. **392**, 45 (1984).
[41] J.C. Juanes-Marcos, S.C. Althorpe, and E. Wrede, Science **309**, 1227 (2005).

[42] A. Migani, L. Blancafort, M.A. Robb, and A.D. DeBellis, J. Am. Chem. Soc. **130**, 6932 (2008).
[43] Q.S. Li, D. Mendive-Tapia, M.J. Paterson, A. Migani, M.J. Bearpark, M.A. Robb, and L. Blancafort, Chem. Phys. **377**, 60 (2010).
[44] S.Y. Grebenshchikov, Z.W. Qu, H. Zhu, and R. Schinke, Phys. Chem. Chem. Phys. **9**, 2044 (2007).
[45] D. Picconi and S.Y. Grebenshchikov, J. Chem. Phys. **141**, 074311 (2014).
[46] M. Böhm, J. Tatchen, D. Krügler, K. Kleinermanns, M.G.D. Nix, T.A. LeGreve, T.S. Zwier, and M. Schmitt, J. Phys. Chem. A **113**, 2456 (2009).
[47] G.M.D. Roberts, D.J. Hadden, L.T. Bergendahl, A.M. Wenge, S.J. Harris, T.N.V. Karsili, M.N.R. Ashfold, M.J. Paterson, and V.G. Stavros, Chem. Sci. **4**, 993 (2013).
[48] G.M. Roberts, C.A. Williams, J.D. Young, S. Ullrich, M.J. Paterson, and V.G. Stavros, J. Am. Chem. Soc. **134**, 12578 (2012).
[49] C.P. Rodrigo, C. Zhou, and H. Reisler, J. Phys. Chem. A **117**, 12049 (2013).
[50] A.S. Chatterley, J.D. Young, D. Townsend, J.M. Żurek, M.J. Paterson, G.M. Roberts, and V.G. Stavros, Phys. Chem. Chem. Phys. **15**, 6879 (2013).
[51] Y. Zhang, K. Yuan, S. Yu, and X. Yang, J. Phys. Chem. Lett. **1**, 475 (2010).
[52] M. Nakamura, P.-Y. Tsai, T. Kasai, K.-C. Lin, F. Palazzetti, A. Lombardi, and V. Aquilanti, Faraday Discuss. **177**, 77 (2015).
[53] M.L. Hause, Y. Heidi Yoon, A.S. Case, and F.F. Crim, J. Chem. Phys. **128**, 104307 (2008).
[54] F.F. Crim, Annu. Rev. Phys. Chem. **44**, 397 (1993).
[55] A. Bach, J.M. Hutchison, R.J. Holiday, and F.F. Crim, J. Phys. Chem. A **107**, 10490 (2003).
[56] M.L. Hause, Y.H. Yoon, and F.F. Crim, Mol. Phys. **106**, 1127 (2008); J. Chem. Phys. **125**, 174309 (2006).
[57] Y. Arasaki, K. Takatsuka, K. Wang, and V. McKoy, J. Chem. Phys. **132**, 124307 (2010).
[58] H.J. Worner, J.B. Bertrand, B. Fabre, J. Higuet, H. Ruf, A. Dubrouil, S. Patchkovskii, M. Spanner, Y. Mairesse, V. Blanchet, E. Mevel, E. Constant, P.B. Corkum, and D.M. Villeneuve, Science **334**, 208 (2011).
[59] V. Vallet, Z. Lan, S. Mahapatra, A.L. Sobolewski, and W. Domcke, J. Chem. Phys. **123**, 144307 (2005).
[60] D. Polli, P. Altoè, O. Weingart, K.M. Spillane, C. Manzoni, D. Brida, G. Tomasello, G. Orlandi, P. Kukura, R.A. Mathies, M. Garavelli, and G. Cerullo, Nature **467**, 440 (2010).
[61] R.A. Livingstone, J.O.F. Thompson, M. Iljina, R.J. Donaldson, B.J. Sussman, M.J. Paterson, and D. Townsend, J. Chem. Phys. **137**, 184304 (2012).
[62] A.M.D. Lee, J.D. Coe, S. Ullrich, M.L. Ho, S.J. Lee, B.M. Cheng, M.Z. Zgierski, I.-C. Chen, T.J. Martinez, and A. Stolow, J. Phys. Chem. A **111**, 11948 (2007).
[63] O. Schalk, A.E. Boguslavskiy, and A. Stolow, J. Phys. Chem. A **114**, 4058 (2010).
[64] A.D.G. Nunn, R.S. Minns, R. Spesyvtsev, M.J. Bearpark, M.A. Robb, and H.H. Fielding, Phys. Chem. Chem. Phys. **12**, 15751 (2010).
[65] M. Araújo, B. Lasorne, A.L. Magalhães, M.J. Bearpark, and M.A. Robb, J. Phys. Chem. A **114**, 12016 (2010).
[66] J.S. Lim and S.K. Kim, Nat. Chem. **2**, 627 (2010).
[67] M.N.R. Ashfold, G.A. King, D. Murdock, M.G.D. Nix, T.A.A. Oliver, and A.G. Sage, Phys. Chem. Chem. Phys. **12**, 1218 (2010).
[68] J.S. Lim, I.S. Lim, K.-S. Lee, D.-S. Ahn, Y.S. Lee, and S.K. Kim, Angew. Chem. Int. Ed. **45**, 6290 (2006).
[69] I.S. Lim, J.S. Lim, Y.S. Lee, and S.K. Kim, J. Chem. Phys. **126**, 034306 (2007).
[70] J.S. Lim, Y.S. Lee, and S.K. Kim, Angew. Chem. Int. Ed. **47**, 1853 (2008).
[71] D.-S. Ahn, J. Lee, J.-M. Choi, K.-S. Lee, S.J. Baek, K. Lee, K.-K. Baeck, and S.K. Kim, J. Chem. Phys. **128**, 224305 (2008).
[72] J.S. Lim, H. Choi, I.S. Lim, S.B. Park, Y.S. Lee, and S.K. Kim, J. Phys. Chem. A **113**, 10410 (2009).

[73] S. Han, J.S. Lim, J.-H. Yoon, J. Lee, S.-Y. Kim, and S.K. Kim, J. Chem. Phys. **140**, 054307 (2014).
[74] J.-H. Yoon, K.C. Woo, and S.K. Kim, Phys. Chem. Chem. Phys. **16**, 8949 (2014).
[75] S. Han, H.S. You, S.-Y. Kim, and S.K. Kim, J. Phys. Chem. A **118**, 6940 (2014).
[76] W. Fuß, T. Schikarski, W.E. Schmid, S. Trushin, and K.L. Kompa, Chem. Phys. Lett. **262**, 675 (1996).
[77] S.A. Trushin, W. Fuß, T. Schikarski, W.E. Schmid, and K.L. Kompa, J. Chem. Phys. **106**, 9386 (1997).
[78] C.-K. Ni, C.-M. Tseng, M.-F. Lin, and Y.A. Dyakov, J. Phys. Chem. B **111**, 12631 (2007).
[79] C.L. Ward and C.G. Elles, J. Phys. Chem. Lett. **3**, 2995 (2012).
[80] M.N.R. Ashfold, B. Cronin, A.L. Devine, R.N. Dixon, and M.G.D. Nix, Science **312**, 1637 (2006).
[81] Z. Lan, W. Domcke, V. Vallet, A.L. Sobolewski, and S. Mahapatra, J. Chem. Phys. **122**, 224315 (2005).
[82] M.G.D. Nix, A.L. Devine, B. Cronin, R.N. Dixon, and M.N.R. Ashfold, J. Chem. Phys. **125**, 133318 (2006).
[83] R.N. Dixon, T.A.A. Oliver, and M.N.R. Ashfold, J. Chem. Phys. **134**, 194303 (2011).
[84] M.G.D. Nix, A.L. Devine, R.N. Dixon, and M.N.R. Ashfold, Chem. Phys. Lett. **463**, 305 (2008).
[85] G.M. Roberts, A.S. Chatterley, J.D. Young, and V.G. Stavros, J. Phys. Chem. Lett. **3**, 348 (2012).
[86] A. Iqbal, L.-J. Pegg, and V.G. Stavros, J. Phys. Chem. A **112**, 9531 (2008).
[87] A. Iqbal, M.S.Y. Cheung, M.G.D. Nix, and V.G. Stavros, J. Phys. Chem. A **113**, 8157 (2009).
[88] M. Abe, Y. Ohtsuki, Y. Fujimura, Z. Lan, and W. Domcke, J. Chem. Phys. **124**, 224316 (2006).
[89] O.P.J. Vieuxmaire, Z. Lan, A.L. Sobolewski, and W. Domcke, J. Chem. Phys. **129**, 224307 (2008).
[90] C.-M. Tseng, Y.T. Lee, and C.-K. Ni, J. Chem. Phys. **121**, 2459 (2004).
[91] G.A. King, T.A.A. Oliver, M.G.D. Nix, and M.N.R. Ashfold, J. Phys. Chem. A **113**, 7984 (2009).
[92] M.N.R. Ashfold, A.L. Devine, R.N. Dixon, G.A. King, M.G.D. Nix, and T.A.A. Oliver, Proc. Nat. Acad. Sci. **105**, 12701 (2008).
[93] A.L. Devine, M.G.D. Nix, B. Cronin, and M.N.R. Ashfold, Phys. Chem. Chem. Phys. **9**, 3749 (2007).
[94] G.A. King, A.L. Devine, M.G.D. Nix, D.E. Kelly, and M.N.R. Ashfold, Phys. Chem. Chem. Phys. **10**, 6417 (2008).
[95] G.A. Pino, A.N. Oldani, E. Marceca, M. Fujii, S.I. Ishiuchi, M. Miyazaki, M. Broquier, C. Dedonder, and C. Jouvet, J. Chem. Phys. **133**, 124313 (2010).
[96] D.J. Hadden, C.A. Williams, G.M. Roberts, and V.G. Stavros, Phys. Chem. Chem. Phys. **13**, 4494 (2011).
[97] C.-M. Tseng, Y.T. Lee, and C.-K. Ni, J. Phys. Chem. A **113**, 3881 (2009).
[98] C.-M. Tseng, Y.A. Dyakov, C.-L. Huang, A.M. Mebel, S.H. Lin, Y.T. Lee, and C.-K. Ni, J. Am. Chem. Soc. **126**, 8760 (2004).
[99] G.A. King, T.A.A. Oliver, and M.N.R. Ashfold, J. Chem. Phys. **132**, 214307 (2010).
[100] R. Montero, A.P. Conde, V. Ovejas, R. Martínez, F. Castaño, and A. Longarte, J. Chem. Phys. **135**, 054308 (2011).
[101] R. Spesyvtsev, O.M. Kirkby, M. Vacher, and H.H. Fielding, Phys. Chem. Chem. Phys. **14**, 9942 (2012).
[102] R. Spesyvtsev, O.M. Kirkby, and H.H. Fielding, Faraday Discuss. **157**, 165 (2012).
[103] D.A. Blank, S.W. North, and Y.T. Lee, Chem. Phys. **187**, 35 (1994).
[104] J. Wei, A. Kuczmann, J. Riedel, F. Renth, and F. Temps, Phys. Chem. Chem. Phys. **5**, 315 (2003).

[105] J. Wei, J. Riedel, A. Kuczmann, F. Renth, and F. Temps, Faraday Discuss. **127**, 267 (2004).
[106] B. Cronin, M.G.D. Nix, R.H. Qadiri, and M.N.R. Ashfold, Phys. Chem. Chem. Phys. **6**, 5031 (2004).
[107] H. Lippert, H.H. Ritze, I.V. Hertel, and W. Radloff, Phys. Chem. Chem. Phys. **5**, 1423 (2004).
[108] Z. Lan, A. Dupays, V. Vallet, S. Mahapatra, and W. Domcke, J. Photochem. Photobiol. A **190**, 177 (2007).
[109] M. Barbatti, J. Pittner, M. Pederzoli, U. Werner, R. Mitrić, V. Bonačić-Koutecký, and H. Lischka, Chem. Phys. **375**, 26 (2010).
[110] S. Faraji, M. Vazdar, V.S. Reddy, M. Eckert-Maksic, H. Lischka, and H. Köppel, J. Chem. Phys. **135**, 154310 (2011).
[111] A.L. Sobolewski and W. Domcke, Chem. Phys. **259**, 181 (2000).
[112] T.S. Venkatesan, S.G. Ramesh, Z. Lan, and W. Domcke, J. Chem. Phys. **136**, 174312 (2012).
[113] A.L. Devine, M.G.D. Nix, R.N. Dixon, and M.N.R. Ashfold, J. Phys. Chem. A **112**, 9563 (2008).
[114] T.A.A. Oliver, G.A. King, D.P. Tew, R.N. Dixon, and M.N.R. Ashfold, J. Phys. Chem. A **116**, 12444 (2012).
[115] H. An, H. Choi, Y.S. Lee, and K.K. Baeck, Chem. Phys. Chem. **16**, 1529 (2015).
[116] M.N.R. Ashfold, G.A. King, M.G.D. Nix, and T.A.A. Oliver, in *Handbook of High Resolution Spectroscopy*, edited by M. Quack and F. Merkt (Wiley, Chichester, UK, 2009).
[117] G.M. Roberts and V.G. Stavros, Chem. Sci. **5**, 1698 (2014).
[118] C.-W. Cheng, Y.-P. Lee, and H.A. Witek, J. Phys. Chem. A **112**, 11998 (2008).
[119] J.B. Kim, T.I. Yacovitch, C. Hock, and D.M. Neumark, Phys. Chem. Chem. Phys. **13**, 17378 (2011).
[120] A.T.J.B. Eppink and D.H. Parker, Rev. Sci. Instrum. **68**, 3477 (1997).
[121] M.N.R. Ashfold, N.H. Nahler, A.J. Orr-Ewing, O.P.J. Vieuxmaire, R.L. Toomes, T.N. Kitsopoulos, I.A. Garcia, D.A. Chestakov, S.-M. Wu, and D.H. Parker, Phys. Chem. Chem. Phys. **8**, 26 (2006).
[122] A.J.R. Heck and D.W. Chandler, Annu. Rev. Phys. Chem. **46**, 335 (1995).
[123] D. Townsend, W. Li, S.K. Lee, R.L. Gross, and A.G. Suits, J. Phys. Chem. A **109**, 8661 (2005).
[124] K.-S. Lee, J.-S. Lim, D.S. Ahn, K.-W. Choi, S.K. Kim, and Y.S. Choi, J. Chem. Phys. **124**, 124307 (2006).
[125] V. Dribinski, A. Ossadtchi, V.A. Mandelshtam, and H. Reisler, Rev. Sci. Instrum. **73**, 2634 (2002).
[126] G.A. Garcia, L. Nahon, and I. Powis, Rev. Sci. Instrum. **75**, 4989 (2004).
[127] L. Zhu and P. Johnson, J. Chem. Phys. **94**, 5769 (1991).
[128] H. Krause and H.J. Neusser, J. Chem. Phys. **97**, 5923 (1992).
[129] D.M. Neumark, J. Phys. Chem. A **112**, 13287 (2008).
[130] S.J. Baek, K.-W. Choi, Y.S. Choi, and S.K. Kim, J. Chem. Phys. **118**, 11040 (2003).
[131] D.-S. Ahn, J. Lee, Y.C. Park, Y.S. Lee, and S.K. Kim, J. Chem. Phys. **136**, 024306 (2012).
[132] A.M. Gardner, A.M. Green, V.M. Tamé-Reyes, K.L. Reid, J.A. Davies, V.H.K. Parkes, and T.G. Wright, J. Chem. Phys. **140**, 114308 (2014).
[133] J.A. Davies, A.M. Green, A.M. Gardner, C.D. Withers, T.G. Wright, and K.L. Reid, Phys. Chem. Chem. Phys. **16**, 430 (2014).
[134] H.S. You, S. Han, J.S. Lim, and S.K. Kim, J. Phys. Chem. Lett. **6**, 3202 (2015).
[135] R.N. Zare, Mol. Photochem. **4**, 1 (1972).
[136] A.D. Becke, Phys. Rev. A. **38**, 3098 (1988).
[137] H. Choi, Y.C. Park, Y.S. Lee, H. An, and K.K. Baeck, Chem. Phys. Lett. **580**, 32 (2013).
[138] D.J. Nesbitt and R.W. Field, J. Phys. Chem. **100**, 12735 (1996).

[139] P. Mulder, O. Mozenson, S. Lin, C.E.S. Bernardes, M.E. Minas da Piedade, A.F.L.O.M. Santos, M.A.V. Ribeiro da Silva, G.A. DiLabio, H.-G. Korth, and K.U. Ingold, J. Phys. Chem. A **110**, 9949 (2006).
[140] T. Vondrák, S.-I. Sato, V. Špirko, and K. Kimura, J. Phys. Chem. A **101**, 8631 (1997).
[141] A.T.J.B. Eppink and D.H. Parker, J. Chem. Phys. **110**, 832 (1999).
[142] D.F. McMillen and D.M. Golden, Annu. Rev. Phys. Chem. **33**, 493 (1982).
[143] S.J. Baek, K.-W. Choi, Y.S. Choi, and S.K. Kim, J. Chem. Phys. **117**, 2131 (2002).
[144] H.J. Werner and P.J. Knowles, J. Chem. Phys. **82**, 5053 (1985).
[145] P.J. Knowles and H.-J. Werner, Chem. Phys. Lett. **115**, 259 (1985).
[146] P.F. Bernath, *Spectran of Atoms and Molecules*, 2nd ed. (Oxford University Press, New York, 2005).
[147] J. von Neumann and E. Wigner, Physik. Z **30**, 467 (1929).
[148] L.S. Cederbaum, Phys. Rev. Lett. **90**, 013001 (2003).
[149] L.S. Cederbaum, R.S. Friedman, V.M. Ryaboy, and N. Moiseyev, Phys. Rev. Lett. **90**, 013001 (2003).
[150] D.-S. Ahn, S.-Y. Kim, G.-I. Lim, S. Lee, Y.S. Choi, and S.K. Kim, Angew. Chem. Int. Ed. **49**, 1244 (2010).
[151] J. Lee, S.-Y. Kim, and S.K. Kim, J. Phys. Chem. A **118**, 1850 (2014).
[152] C.S. Parmenter and B.M. Stone, J. Chem. Phys. **84**, 4710 (1986).
[153] J.A. Davies, A.M. Green, A.M. Gardner, C.D. Withers, T.G. Wright, and K.L. Reid, Phys. Chem. Chem. Phys. **16**, 430 (2014).
[154] P. Celani and H.-J. Werner, J. Chem. Phys. **119**, 5044 (2003).
[155] B.J. Sussman, D. Townsend, M.Y. Ivanov, and A. Stolow, Science **314**, 278 (2006).
[156] C.E. Hamilton, J.L. Kinsey, and R.W. Field, Annu. Rev. Phys. Chem. **37**, 493 (1986).
[157] F. Filsinger, J. Küpper, G. Meijer, J.L. Hansen, J. Maurer, J.H. Nielsen, L. Holmegaard, and H. Stapelfeldt, Angew. Chem. Int. Ed. **48**, 6900 (2009).
[158] F. Filsinger, J. Küpper, G. Meijer, L. Holmegaard, J.H. Nielsen, I. Nevo, J.L. Hansen, and H. Stapelfeldt, J. Chem. Phys. **131**, 064309 (2009).
[159] J. Küpper, F. Filsinger, and G. Meijer, Faraday Discuss. **142**, 155 (2009).
[160] Y.-P. Chang, K. Dlugolecki, J. Küpper, D. Rosch, D. Wild, and S. Willitsch, Science 342, 98 (2013).
[161] M.E.Corrales, J.González Vázquez, G.Balerdi, I.R.Solá, R.de Nalda, and L.Bañares, Nat. Chem. **6**, 785 (2014).